Damage mechanisms of material in single-cone scratching

Linfa Peng[1]*, Zhutian Xu[1], Mengyun Mao[1,2], Xinmin Lai[1], Ming Wang Fu[2#]

[1] State Key Laboratory of Mechanical System and Vibration, Shanghai Jiao Tong University, Shanghai 200240, People's Republic of China

[2] Department of Mechanical Engineering, The Hong Kong Polytechnic University, Hung Hom, Kowloon, Hong Kong

*: Email: penglinfa@sjtu.edu.cn, Tel: 86 21 3420 6303

[#] : Email: mmmwfu@polyu.edu.hk, Tel: 852 2766 5527

Abstract

The scratching test has been a key method to characterize the basic mechanics of material in vast scenarios. Although attentions have been paid to this field for decades, a comprehensive analytical framework, which includes material flow, fracture initiation and crack propagation, is still missing. The wide application of scratching test and the accurate description of material behaviors in friction is thus limited. To address the problem, an analytical frame model was established in this study. The strain distribution and pileup ratio in the symmetry section of the front ridge was calculated. Furthermore, the ductile fracture law was also included to predict the mechanism and the initiation location of fracture in the scratching process. The predictive results were further validated by SEM observations of the scratched grooves. The effects of cone angle and material properties on the damage mechanisms of material in the scratching process were studied. It was revealed that the damage mechanism changes from shear failure to tensile failure, and further to plastic deformation with the increase of cone angle and the ratio of yielding stress to Young's modulus. Finally, a map of the damage mechanism of material in the scratching process was obtained by utilizing the developed model. The presented works are meaningful to the

The following publication Peng, L., Xu, Z., Mao, M., Lai, X., and Fu, M. W. (February 2, 2021). "Damage Mechanisms of Material in Single-Cone Scratching." ASME. J. Manuf. Sci. Eng. June 2021; 143(6): 061013 is available at https://doi.org/10.1115/1.4049478.

understanding of material behavior in ploughing, and helpful in predicting and controlling the surface quality of those parts subject to different machining and forming processes.

Keywords: Scratching process, damage mechanism, ductile fracture, contact mechanics.

1 Introduction

Traditionally, the scratching test has been regarded as a mechanics-of-materials test for property characterization [1]. However, it is also an effective approach to investigate the behaviors of materials during ploughing and help us to understand the tool-workpiece interfacial friction behavior [2], surface hardness [3], fracture [4] and material removal mechanisms [5]. An accurate description of the ploughing effect is thus critical in various machining processes such as milling, drilling and grinding. In addition, micro scratching is also a key factor affecting the friction and wear in various forming processes. As the fabrication accuracy and surface quality requirements increase with the development of modern industries, the importance of a thorough understanding of the ploughing effect is self-evident.

The scratching or ploughing process can be described as a hard indenter or asperity moving across a softer surface to produce a groove. During the process, severe plastic deformation, cracks and even material detachment can be induced by the movement of indenter. By identifying whether a crack or fracture occurs in the soft or ductile material, the process can be distinguished into two different types, termed mild scratching and severe scratching processes. In the mild scratching, deformation is governed by the bulk constitutive properties, typically plastic for metallic materials or non-linearly viscoelastic for polymers, without chipping, spalling or delaminating. While the severe scratching occurs if the material toughness is sufficiently low and the formation of cracks takes place [6]. In some prior works, the scratching process is also divided into three types, namely rubbing, wear, and cutting. Rubbing can be regarded as the mild scratching. The wear scratching means fracture and material removal take place. If the removed material is able to form continuous chips, the scratching was treated as the cutting process [7].

The mechanism of scratching process for ductile materials can transform from deformation to fracture due to the geometry of scratching tools, the indented depth and the properties of base materials. Many prior experimental arts have revealed that the complicated behavior of materials during the scratching process is significantly affected by the process parameters such as attack angle, penetration depth, and mechanical properties of material. Among them, the experimental works conducted by Sedriks and Mulhearn [8] on the scratching of pure metals with pyramidal tools showed the attack angle of the indenter, which is the angle between the leading edge or face and the direction of sliding, must exceed a critical value until material detachment takes place. Similar conclusions were obtained by scratching ductile materials with rigid asperities of different shapes [9, 10]. Besides the attack angle, the scratching mechanism is also revealed to change from ploughing to wedge-forming, and then to the cutting mode as the degree of penetration increases with the help of in-situ scanning electron microscope (SEM) [11]. Moreover, the critical penetration degree for the transition from the ploughing mode to the wedge-forming mode was independent of the hardness. While the critical penetration degree for the transition from wedge-forming to cutting decreases with the increasing hardness. Recently, it was reported that the mode of failure (fracture vs. plastic yielding) is influenced by the material properties as well as the geometry of scratching tools [4, 12] .

To determine the mechanism of scratching, attentions were paid to the theoretical modelling of the process. Williams [13] made two principal assumptions for the elementary model of the scratching or ploughing process: The resistance to penetration of the material is a material constant which is independent of the loading directions. The effect of adhesive friction is independent of the

involving deformation. Untill now, this approach is still widely used due to its simple formation [14]. However, the evolution of free surface as well as the fracture of material is not able to be considered in those analyses. To overcome the problem, the slip-line field method is employed to model the scratching process. Challen and Oxley [15] established the slip-line field of a wedge-shaped tool scratching a deformable flat in plane strain condition. Three different models were established based on that to describe the rubbing, wear and cutting modes respectively. In addition to Challen and Oxley's work, a new slip-line field approach was established by introducing the built-up edge on the front side of the indenter by Yin and Komvopoulos [16]. It should be noticed that the slip-line field method is only available in two-dimensional scenarios. In addition, the method demands the indenter to climb upwards to the exact level of the free surface. Otherwise the scratched material must be removed. Obviously, the method could only partially reflect the material behaviors in scratching tests.

Another traditional way is the upper bound method, which assumes rigid-perfectly plastic material accommodates the movement of indenter by moving around as a series of rigid blocks, creating discontinuities in the tangential components of velocities at the interfaces. Both the cutting and ploughing modes of scratching processes [9] with different shaped tools, such as pyramid [17], cone [18] and generalized asperity [19, 20] were modeled. By considering the stagnant zone formed ahead of tool, the mixed-mode ductile material removal with a conical tool was investigated by Wang and Subhash [21] and the stagnant zone in the model plays a negative role in the removal of material. The application of upper boundary method requires the surface configuration of the plastic zone is known as initio. However, the assumption could not hold in the scratching process since the material is bounded by a stress-free surface whose shape is not

controlled by the tool. Moreover, the mode of deformation, plasticity or fracture, must be assumed as known factors. Hence how the scratching behaviors vary under different conditions could not be predicted.

A number of simulation studies based on finite element (FE) method, molecular dynamic (MD), etc. have recently been conducted to examine the effect of flow stress and tip geometry on the scratch response. Base on the FE simulations, one-cone scratching process on elastic perfectly plastic materials, and compared plastic strains of different materials during the scratching process was studied by Bucaille and Felder [22]. They found the elastic recovery on the rear side of the indenter reduces the scratching resistance of the materials with a rheological factor smaller than 100. Single-pass scratch tests on bilinear elastic–plastic materials with a conical indenter were simulated to study the influence of interfacial friction coefficient and the apical angle of the indenter on the induced tangential and normal forces by Subhash and Zhang [23]. Similarly, the effect of flow strength and strain hardening on the response to steady-state frictional sliding with a conical indenter was investigated by Bellemare et al. [24]. Single grit scratching simulations were performed by Zhang et al. to study the relationship between the cutting energy and the material removal rate [25]. Following that, A 3D multi-scratch FE model was established based on Abaqus using the Johnson-Cook criteria by Elwasli et al. [26]. Crystal plasticity FE method was adopted to investigate the nanoscratching of copper by Wang et al. [27]. The coupling effects of crystallographic orientation and probe geometry were revealed to affect the load-displacement curve and pile-up topography. MD has also been employed to investigate the nano-indentation and scratch process at even smaller length scales [28-30]. New simulation methods including smooth particle hydrodynamics [12] and material point method [10] are also attracting a lot of attention.

However, the severe deformation during scratching has presented an evident difficulty for the different simulation researches. The accuracy is hindered by the different simulation problems such as mesh distortion, strong strain gradient effects, computation explosion, etc. Hence the fracture mechanism in the scratch process is still not clear.

According to the literature review, an appropriate analytical framework, which includes material flow, fracture initiation and crack propagation, is an urgency for the wide application of scratching test and for the accurate description of material behaviors in friction [10, 24]. Recently, a series of work were done by Akono and Ulm [1, 4] , they derived general scratch force scaling relations for axisymmetric scratch probes defined by single variable monomial functions and used the relations to define fracture criteria with and without consideration of the development of shear stresses at the probe–material interface. In their models, the fracture propagates when the released energy extended the critical fracture energy. And the final fracture criterion is related to the geometry of indenter, the toughness of material and the indented depth. However, limitations of the criterion are concluded by the authors that the effect of large (eventually inelastic) deformation on the hardening behavior ahead of the scratch probe cannot be captured since a linear elastic behavior of solid is assumed. The approach is thus restricted to elastic-brittle materials. Moreover, the model assumed the scratch probe is surrounded by a crack plane. Hence the criterion is considered to be more accurate to predict the propagation of fracture than to describe the initiation of fracture.

The present study deals with a more essential problem, i.e., whether and how the fracture is generated by the movement of rigid cone in the scratching processes with different cone angles, penetration depth and material properties. It is important to find an appropriate theory or method

to study the scratching process. In order to address the problem, the material in front of the rigid cone is simplified into a series of line elements, and the increment of strain as a function of cone angle was deduced according to the elongation of the line elements and contact mechanics. With the help of iteration calculation, the strain distribution as a function of sliding distance, cone angle and mechanical property was obtained based on the strain field increment. By making the strain equal to the fracture strain, the critical cone angle for the transition from deformation to fracture as well as the influence of material properties on the angle was finally determined. The results are meaningful to the understanding of material deformation and fracture behaviors in ploughing. The model established in this work could be applied in different cutting and forming processes to predict the surface conditions, the generation of surficial micro cracks, the wear behaviors etc. under different tool asperities conditions. The model could also be easily incorporated in the mechanism-based machine learning systems of different manufacturing processes for the process design and optimization.

2 Analytical approach

Previous studies have defined two scratch modes namely cutting and ploughing based on the material flow direction. A cutting mode scratch is accomplished with the chip being formed where the particle usually flow upwards along the tool surface so as to detach from the surface of the workpiece, while a ploughing mode scratch is formed with the material being displaced by the particles usually moving either downwards or sideways along the tool surface without the chip generated [21]. Obviously, in cutting mode, fracture is the main mechanism of damage, and in ploughing mode, the mechanism of damage is depending on the process parameters. Thus the analysis mainly focuses on the ploughing mode in this study.

2.1 Theoretical background

The physical explanation of fracture mechanism in scratching process is still not clear due to the complex stress condition caused by the sliding of the tool. The existing explanations in the traditional analysis are always phenomenon based. For example, in upper bound analysis, the fracture is usually assumed to be formed on the front side or the lateral side of the tool according to De Vathaire et al. [31]. In slip-line field analysis, fracture is considered to happen when the attack angle is larger than the friction angle. In this study, the initiation of fracture is defined as the transformation of material from continuous to discontinuous. Thus, the material is firstly assumed to be a continuum.

In the ploughing process, the plastic flow of a particle on the interface of indenter and material can be divided into two components according to the contact interface, namely the normal component, d_n, and the tangential component, d_t, given by Eq. (1).

$$\begin{cases} d_n = d_s \sin\alpha' \\ d_t = d_s \cos\alpha' \\ \alpha' = f(\alpha, m) \end{cases} \tag{1}$$

Here, α is the semi-angle of the indenter, and m is friction factor on the interface.

With the sliding of indenter begins, both the components of d_n and d_t increase. If d_t is greater than the distance for the particle to pass the widest section of the indenter, the particle can climb over the indenter. Meanwhile, the increase of d_n also leads to the increasing strain of the particle. Thus a criterion of fracture can be interpreted as if the strain of the particle is greater than the fracture strain before it climbs over the indenter, fracture can take place in the scratch process. Particularly,

as the deformation of material is extremely nonlinear, the strain field could be obtained by iterating the strain increment under small movement increment.

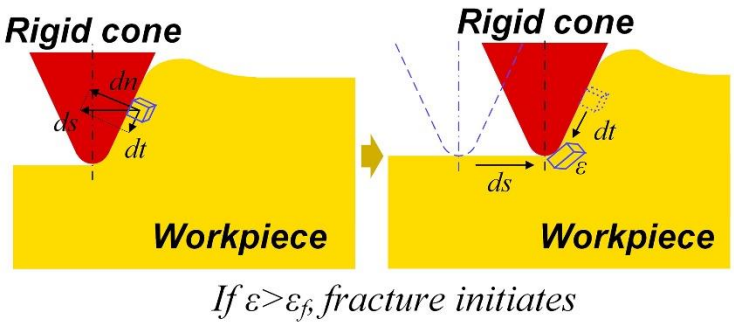

Fig. 1 Fracture criterion in ploughing.

2.2 Strain increment induced by a small increment of scratching

2.2.1 Basic assumptions

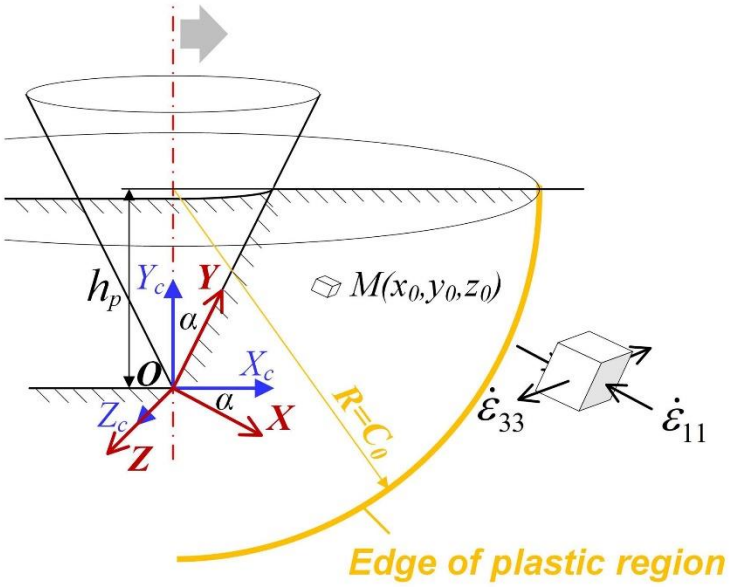

Fig. 2 Schematic of the scratch morphology and relevant global and local coordinate systems during the scratching process.

Consider a rigid cone scratching a ductile flat, the interaction between the tool and the deformed material is shown in Fig. 2. The indented depth is h_p, and the rigid cone slides parallel to the surface of the material with a velocity of V. The global coordinates of $X_cY_cZ_c$ can be established as shown in Fig. 2.

The transition matrix of the coordinates is given as follow:

$$P = \begin{bmatrix} \cos\alpha & 0 & -\sin\alpha \\ 0 & 1 & 0 \\ \sin\alpha & 0 & \cos\alpha \end{bmatrix} \tag{2}$$

The small movement U of cone in the direction of X_c can be divided into a component U_c in X direction and a component U_s in Y direction, respectively. Particularly, U_c can cause the compression deformation, while U_s is the relative slip of the contacting surface. If the contacting surface is well lubricated and the friction is eliminated, the deformation of the scratching material is mainly caused by the compression component, U_c.

For an infinite plane, only the adjacent material is strained by the displacement of cone, and the strain far away from the cone is considered to be 0. Assuming the strain in the deformed region is pure plastic, according to contact mechanics, the shape of plastic deformation region caused by the indentation of a rigid cone into a plastic material can be regarded as a semisphere with the radius [32]:

$$C = \left[\frac{E\tan\alpha}{6(1-\nu)Y} + \frac{2(1-2\nu)}{3(1-\nu)} \right]^{\frac{1}{3}} h_p \tan\alpha \tag{3}$$

Here, E, Y and ν are the Young's modulus, yielding stress and Possion's ratio of material, respectively. α is the semi angle of the cone, and h_p is the indented depth.

Thus the boundary of the plastic region in $X_cY_cZ_c$ coordinates can be obtained as follow:

$$x_c^2 + \left(y_c - h_p\right)^2 + z_c^2 = C^2 \tag{4}$$

In *XYZ* system, the boundary is expressed as

$$\left(x + h_p \sin\alpha\right)^2 + \left(y - h_p \cos\alpha\right)^2 + z^2 = C^2 \tag{5}$$

In the plane *z=0*, boundary in *X* direction is obtained as

$$C_0 = \sqrt{C^2 - \left(y_0 - h_p \cos\alpha\right)^2} - h_p \sin\alpha \tag{6}$$

As shown in Fig. 3, line ACB is a random line element of material in front of rigid cone. According to the assumption of continuity, line ACB should be continuous during the scratch, hence the location and shape of line ACB can be illustrated as Fig. 3. During the process, line ACB is elongated by the compression component U_c, while the sliding component U_s makes the line move downward, and finally be passed over by the cone. If no fracture is allowed during the process, the strain on the line should not exceed the fracture strain of the material before it is passed over by the cone.

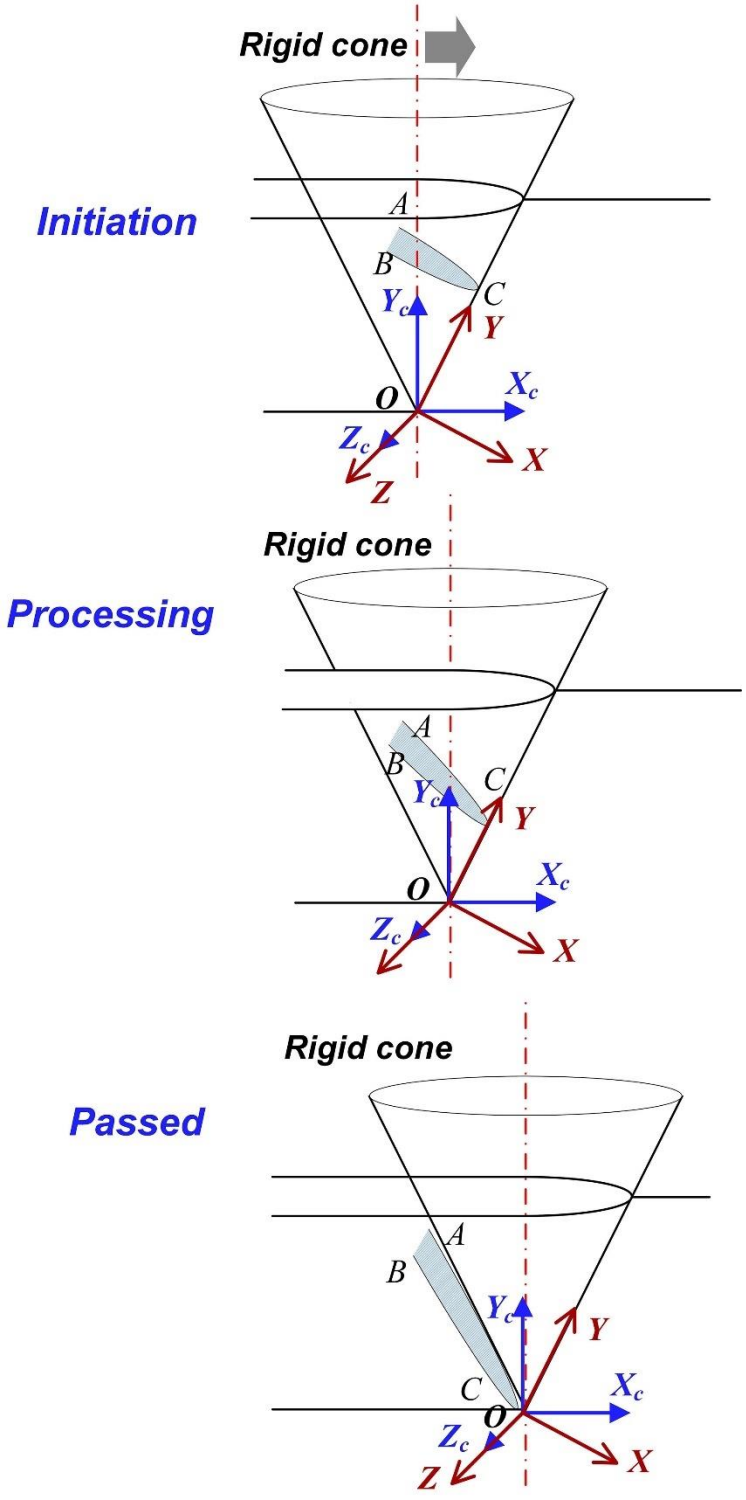

Fig. 3 Evolution of the intersection line ACB.

In tandem with the analysis above, the deformation region can be simplified into a series of line elements, as shown in Fig. 4 (a), based on the shape of cone. Firstly, the deformation region is divided into numerous of sections, which are parallel to the *XOZ* plane. Then, on each section, a series of curves, which are similar to the intersection line of the rigid cone, are drawn, as shown in Fig. 4 (b). As the intersection lines on different sections are similar to each other, the deformation region can be represented by a series of similar line elements.

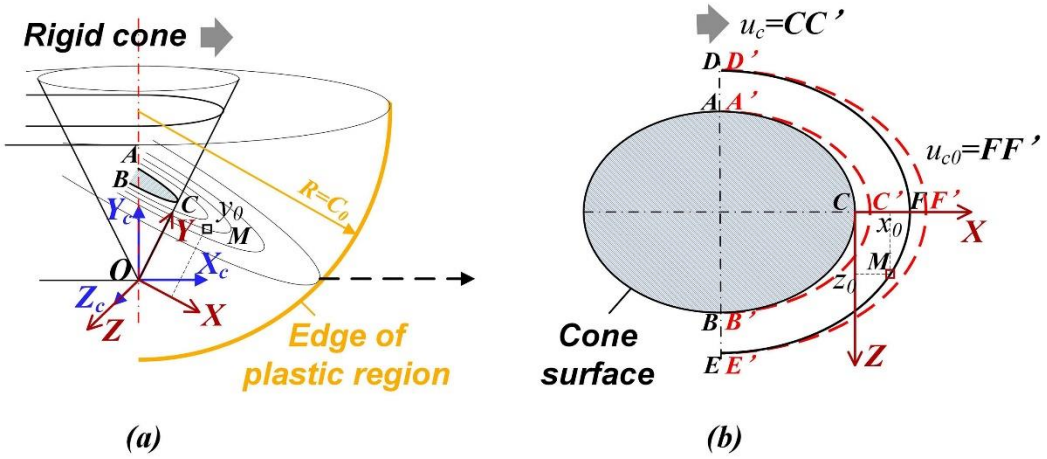

Fig. 4 Schematic illustrations of (a) the Line element simplification, (b) *XZ* plane for a given $y=y_0$.

In the *XYZ* coordinates, the intersection line can be expressed as *z=f(x)*. *M* is a random point in the deformation region with the coordinate values of (x_0, y_0, z_0) which is in the line *DFE*. According to the similarity, line *DFE* can be represented by the coordinate values of *M*.

Considering a cross section as illustrated in Fig. 4 (b) with an arbitrary y_0, an extremely small displacement is applied to the rigid cone. The base material is deformed and line *DFE* is elongated to line *D'F'E'*. Ignoring the effect of adhesion on the contacting surfaces, and taking the advantage

of the extremely small displacement, the following simplifications are made to obtain the strain field:

(1) Lines *DFE* and *D'F'E'* are on the same plane.

(2) Points *D* and *E* are coincident with *D'* and *E'*.

(3) The elongation of Line *DFE* is uniform.

Thus the elongation of line *DFE* can be expressed as follows:

$$\delta l = \frac{l_1 - l_0}{l_0} = \frac{\int_{x_1'}^{x_2} \sqrt{1 + g'(x)^2}\, dx}{\int_{x_1}^{x_2} \sqrt{1 + f'(x)^2}\, dx} - 1 \tag{7}$$

Here, $z=f(x)$ and $z=g(x)$ are the geometric analytical expressions of line *DFE* and *D'F'E'*, respectively.

In *XYZ* system, the coordinate values of the points are represented as $F(x_1,0)$, $F'(x_1',0)$, $D(-x_2,-z_2)$, $E(-x_2,z_2)$. And the following equation is obtained:

$$x_1' - x_1 = u_{c0} \tag{8}$$

u_{c0} is the displacement of point *F*, which is a function of *x* coordinate, and smaller than u_c due to the deformation of material. As the strain at the edge of the deformation region is 0, the distribution of the displacement along *x* axis $u_{x\text{-}axis}$ should satisfy the following boundary conditions:

$$\begin{cases} u_{x-axis}(0) = u_c \\ u_{x-axis}(C_0) = 0 \\ u_{x-axis}'(C_0) = 0 \end{cases} \tag{9}$$

Assuming the strain along *x* axis is linearly distributed:

$$u_{x-axis}'(x) = Ax + B \tag{10}$$

Substituting Eq. (10) into Eq. (9), the following expression of displacement can be obtained:

$$u_{x-axis}(x) = \frac{u_c}{C_0^{\,2}} x^2 - \frac{2u_c}{C_0} x + u_c \tag{11}$$

$$u_{c0} = \frac{u_c}{C_0^{\,2}} x_1^{\,2} - \frac{2u_c}{C_0} x_1 + u_c \tag{12}$$

The displacement of a point in the line can be divided into two components, namely the rigid movement in *x* direction and the elongation along the tangential of the line. The direction vector of the elongation component is given as follows:

$$\mathrm{T} = \frac{\left(\frac{\partial\left(f(x)-z\right)}{\partial z}, -\frac{\partial\left(f(x)-z\right)}{\partial x} \right)^T}{\sqrt{\left(\frac{\partial\left(f(x)-z\right)}{\partial z} \right)^2 + \left(\frac{\partial\left(f(x)-z\right)}{\partial x} \right)^2}} \tag{13}$$

Therefore, the displacement *u* of an arbitrary point *M* in the line can be expressed as

$$u = \delta l \cdot l_M \cdot \mathrm{T} + \left(u_{c0}, 0\right)^T \tag{14}$$

Here, l_M is the arc length from *M* to *F*. Based on the displacement, the strain of *M* can be calculated according to the following equations:

$$\varepsilon_x = \frac{\partial u_x}{\partial x} = \frac{\partial \delta l}{\partial x} \cdot l_M \cdot T_x + \delta l \cdot \frac{\partial l_M}{\partial x} \cdot T_x + \delta l \cdot l_M \cdot \frac{\partial T_x}{\partial x} + \frac{\partial u_{c0}}{\partial x} \tag{15}$$

$$\varepsilon_z = \frac{\partial u_z}{\partial z} = \frac{\partial \delta l}{\partial z} \cdot l_M \cdot T_z + \delta l \cdot \frac{\partial l_M}{\partial z} \cdot T_z + \delta l \cdot l_M \cdot \frac{\partial T_z}{\partial z} \tag{16}$$

$$\begin{aligned} \gamma_{xz} = \gamma_{zx} &= \frac{1}{2}\left(\frac{\partial u_x}{\partial z} + \frac{\partial u_z}{\partial x} \right) \\ &= \frac{1}{2}\left(\left(\frac{\partial \delta l}{\partial z} \cdot T_x + \frac{\partial \delta l}{\partial x} \cdot T_z \right) \cdot l_M + \delta l \cdot \left(\frac{\partial l_M}{\partial z} \cdot T_x + \frac{\partial l_M}{\partial x} \cdot T_z \right) + \delta l \cdot l_M \cdot \left(\frac{\partial T_x}{\partial z} + \frac{\partial T_z}{\partial x} \right) + \frac{\partial u_{c0}}{\partial z} \right) \end{aligned} \tag{17}$$

According to assumption (1) and the volume constancy, the other strain components are obtained as follows:

$$\varepsilon_y = -\left(\varepsilon_x + \varepsilon_z\right) = -\left(\frac{\partial \delta l}{\partial x}\cdot T_x + \frac{\partial \delta l}{\partial z}\cdot T_z\right)\cdot l_M - \delta l\cdot\left(\frac{\partial l_M}{\partial x}\cdot T_x + \frac{\partial l_M}{\partial z}\cdot T_z\right) - \delta l\cdot l_M\cdot\left(\frac{\partial T_x}{\partial x} + \frac{\partial T_z}{\partial z}\right) - \frac{\partial u_{c0}}{\partial x} \tag{18}$$

$$\gamma_{xy} = \gamma_{yx} = \frac{1}{2}\left(\frac{\partial u_x}{\partial y} + \frac{\partial u_y}{\partial x}\right) = \frac{1}{2}\left(\frac{\partial \delta l}{\partial y}\cdot T_x\cdot l_M + \delta l\cdot\frac{\partial l_M}{\partial y}\cdot T_x + \delta l\cdot l_M\cdot\frac{\partial T_x}{\partial y} + \frac{\partial u_{c0}}{\partial y}\right) \tag{19}$$

$$\gamma_{zy} = \gamma_{yz} = \frac{1}{2}\left(\frac{\partial u_z}{\partial y} + \frac{\partial u_y}{\partial z}\right) = \frac{1}{2}\left(\frac{\partial \delta l}{\partial y}\cdot T_z\cdot l_M + \delta l\cdot\frac{\partial l_M}{\partial y}\cdot T_z + \delta l\cdot l_M\cdot\frac{\partial T_z}{\partial y}\right) \tag{20}$$

In the $x_c y_c z_c$ system, the strain field is given as:

$$\varepsilon = \mathrm{P}^T\cdot\varepsilon_{xyz} \tag{21}$$

The displacement field is deduced in the following section.

2.2.2 α<45˚ elliptical section

As shown in Fig. 5, when α<45˚, the section of the cone is an ellipse. Thus the equation of the line across $M(x_0,y_0,z_0)$ is expressed as

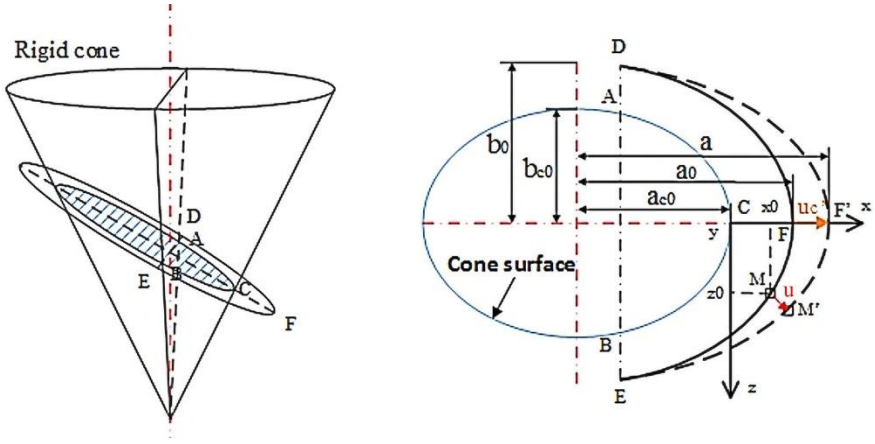

Fig. 5 *XZ* section across an arbitrary point *M* with the semi cone angle α<45˚.

$$\left(\frac{x+a_{c0}}{a_0}\right)^2+\left(\frac{z}{b_0}\right)^2=1 \tag{22}$$

Here, a_0 and b_0 are the semi-major and semi-minor axes of the arbitrary ellipse. a_{c0} is the semi-major axis of the cone section ellipse. According to the geometric similarity, the following relation is obtained:

$$a_{c0}=\frac{1}{2}y_0\tan(2\alpha) \tag{23}$$

$$a_0=\sqrt{\left(x_0+a_{c0}\right)^2+\left(\frac{z_0}{k}\right)^2} \tag{24}$$

$$k=\frac{b_0}{a_0}=\sqrt{1-\tan^2\alpha} \tag{25}$$

After deformation, F is compressed to F', and the coordinate values of E, F and F' are $\left(-y_0\tan\alpha, k\sqrt{{a_0}^2-\left(a_{c0}-y_0\tan\alpha\right)^2}\right)$, $\left(a_0,0\right)$ and $\left(a_0+u_{c0},0\right)$ respectively. After deformation, curve $DF'E$ is still a part of ellipse which can be expressed as:

$$\left(\frac{x+a_{c0}}{a}\right)^2+\left(\frac{z}{b}\right)^2=1 \tag{26}$$

Here, a and b are the semi-major axis and semi-minor axes of the ellipse. Substituting points E and F' into Eq. (26), the following equation can be obtained:

$$\begin{cases} a=a_0+u_{c0} \\ b=k\left(a_0+u_{c0}\right)\sqrt{\dfrac{{a_0}^2-\left(a_{c0}-y_0\tan\alpha\right)^2}{\left(a_0+u_{c0}\right)^2-\left(a_{c0}-y_0\tan\alpha\right)^2}} \end{cases} \tag{27}$$

Here, u_{c0} is the displacement of F. According to Eq. (12), it can be deduced as:

$$u_{c0}=\frac{u_c}{C_0^{\,2}}\left(a_0-a_{c0}\right)^2-\frac{2u_c}{C_0}\left(a_0-a_{c0}\right)+u_c \tag{28}$$

$$\Delta u_{c0}=\frac{2u_c}{a_0C_0}\left(\frac{a_0-a_{c0}}{C_0}-1\right)\begin{pmatrix}x_0+a_{c0}\\ \dfrac{z_0}{k^2}\end{pmatrix} \tag{29}$$

The elongation ratio of curve *DFE* is expressed as follows:

$$\delta l=\frac{a\left[E\left(\sqrt{1-\left(\dfrac{b}{a}\right)^2}\right)-E\left(\theta_c\,|\sqrt{1-\left(\dfrac{b}{a}\right)^2}\right)\right]}{a_0\left[E\left(\sqrt{1-k^2}\right)-E\left(\theta_{c0}\,|\sqrt{1-k^2}\right)\right]}-1 \tag{30}$$

Here, E represents elliptic integral of the second kind. θ_{c0} and θ_c are the argument of point E in the integral before and after deformation, and are expressed as:

$$\begin{aligned}\theta_c&=\arcsin\frac{a_{c0}-y_0\tan\alpha}{a}\\ \theta_{c0}&=\arcsin\frac{a_{c0}-y_0\tan\alpha}{a_0}\end{aligned} \tag{31}$$

$$\begin{cases}\dfrac{\partial\theta_c}{\partial x_0}=-\dfrac{a_{c0}-y_0\tan\alpha}{a\sqrt{a^2-\left(a_{c0}-y_0\tan\alpha\right)^2}}\dfrac{\partial a}{\partial x_0}\\ \dfrac{\partial\theta_c}{\partial z_0}=-\dfrac{a_{c0}-y_0\tan\alpha}{a\sqrt{a^2-\left(a_{c0}-y_0\tan\alpha\right)^2}}\dfrac{\partial a}{\partial z_0}\\ \dfrac{\partial\theta_{c0}}{\partial x_0}=-\dfrac{a_{c0}-y_0\tan\alpha}{a_0\sqrt{a_0^{\,2}-\left(a_{c0}-y_0\tan\alpha\right)^2}}\dfrac{\partial a_0}{\partial x_0}\\ \dfrac{\partial\theta_{c0}}{\partial z_0}=-\dfrac{a_{c0}-y_0\tan\alpha}{a_0\sqrt{a_0^{\,2}-\left(a_{c0}-y_0\tan\alpha\right)^2}}\dfrac{\partial a_0}{\partial z_0}\end{cases} \tag{32}$$

$$\Delta\delta l = \frac{1}{a_0\left[E\left(\sqrt{1-k^2}\right)-E\left(\theta_{c0}\,|\,\sqrt{1-k^2}\right)\right]}\begin{pmatrix} \dfrac{\partial\left(a\left[E\left(\sqrt{1-\left(\frac{b}{a}\right)^2}\right)-E\left(\theta_c\,|\,\sqrt{1-\left(\frac{b}{a}\right)^2}\right)\right]\right)}{\partial x_0}-\ldots \\ (\delta l+1)\left(\dfrac{\partial a_0}{\partial x_0}\left[E\left(\sqrt{1-k^2}\right)-E\left(\theta_{c0}\,|\,\sqrt{1-k^2}\right)\right]- a_0\sqrt{1-(1-k^2)\sin^2\theta_{c0}}\,\dfrac{\partial\theta_{c0}}{\partial x_0}\right) \\ \dfrac{\partial\left(a\left[E\left(\sqrt{1-\left(\frac{b}{a}\right)^2}\right)-E\left(\theta_c\,|\,\sqrt{1-\left(\frac{b}{a}\right)^2}\right)\right]\right)}{\partial z_0}-\ldots \\ (\delta l+1)\left(\dfrac{\partial a_0}{\partial z_0}\left[E\left(\sqrt{1-k^2}\right)-E\left(\theta_{c0}\,|\,\sqrt{1-k^2}\right)\right]- a_0\sqrt{1-(1-k^2)\sin^2\theta_{c0}}\,\dfrac{\partial\theta_{c0}}{\partial z_0}\right) \end{pmatrix} \tag{33}$$

$$
\begin{cases}
\dfrac{\partial\left(a\left[E\left(\sqrt{1-\left(\frac{b}{a}\right)^2}\right)-E\left(\theta_c\,|\sqrt{1-\left(\frac{b}{a}\right)^2}\right)\right]\right)}{\partial x_0}= \\
\left(\dfrac{\partial a_0}{\partial x_0}+\dfrac{\partial u_{c0}}{\partial x_0}\right)\left[E\left(\sqrt{1-\left(\frac{b}{a}\right)^2}\right)-E\left(\theta_c\,|\sqrt{1-\left(\frac{b}{a}\right)^2}\right)\right]+\ldots \\
+a\left(\begin{array}{l}
\dfrac{E\left(\sqrt{1-\left(\frac{b}{a}\right)^2}\right)-F\left(\sqrt{1-\left(\frac{b}{a}\right)^2}\right)}{2\sqrt{1-\left(\frac{b}{a}\right)^2}}\dfrac{\partial\sqrt{1-\left(\frac{b}{a}\right)^2}}{\partial x_0}-\ldots \\
\ldots\sqrt{1-\left(1-\left(\frac{b}{a}\right)^2\right)\sin^2\theta_c}\,\dfrac{\partial\theta_c}{\partial x_0}- \\
\dfrac{E\left(\theta_c\,|\sqrt{1-\left(\frac{b}{a}\right)^2}\right)-F\left(\theta_c\,|\sqrt{1-\left(\frac{b}{a}\right)^2}\right)}{2\sqrt{1-\left(\frac{b}{a}\right)^2}}\dfrac{\partial\sqrt{1-\left(\frac{b}{a}\right)^2}}{\partial x_0}
\end{array}\right) \\
\dfrac{\partial\left(a\left[E\left(\sqrt{1-\left(\frac{b}{a}\right)^2}\right)-E\left(\theta_c\,|\sqrt{1-\left(\frac{b}{a}\right)^2}\right)\right]\right)}{\partial z_0}= \\
\left(\dfrac{\partial a_0}{\partial z_0}+\dfrac{\partial u_{c0}}{\partial z_0}\right)\left[E\left(\sqrt{1-\left(\frac{b}{a}\right)^2}\right)-E\left(\theta_c\,|\sqrt{1-\left(\frac{b}{a}\right)^2}\right)\right]+\ldots \\
+a\left(\begin{array}{l}
\dfrac{E\left(\sqrt{1-\left(\frac{b}{a}\right)^2}\right)-F\left(\sqrt{1-\left(\frac{b}{a}\right)^2}\right)}{2\sqrt{1-\left(\frac{b}{a}\right)^2}}\dfrac{\partial\sqrt{1-\left(\frac{b}{a}\right)^2}}{\partial z_0}-\ldots \\
\ldots\sqrt{1-\left(1-\left(\frac{b}{a}\right)^2\right)\sin^2\theta_c}\,\dfrac{\partial\theta_c}{\partial z_0}- \\
\dfrac{E\left(\theta_c\,|\sqrt{1-\left(\frac{b}{a}\right)^2}\right)-F\left(\theta_c\,|\sqrt{1-\left(\frac{b}{a}\right)^2}\right)}{2\sqrt{1-\left(\frac{b}{a}\right)^2}}\dfrac{\partial\sqrt{1-\left(\frac{b}{a}\right)^2}}{\partial z_0}
\end{array}\right)
\end{cases}
\tag{34}
$$

$$\begin{cases} \dfrac{\partial\sqrt{1-\left(\dfrac{b}{a}\right)^2}}{\partial x_0}=\dfrac{2k^2}{\left(a_0+u_{c0}\right)^2-\left(a_{c0}-y_0\tan\alpha\right)^2} \\ \left(\dfrac{\left(a_0{}^2-\left(a_{c0}-y_0\tan\alpha\right)^2\right)\left(a_0+u_{c0}\right)\left(1+\dfrac{\partial u_{c0}}{\partial a_0}\right)}{\left(a_0+u_{c0}\right)^2-\left(a_{c0}-y_0\tan\alpha\right)^2}-a_0\right)\dfrac{\partial a_0}{\partial x_0} \\ \dfrac{\partial\sqrt{1-\left(\dfrac{b}{a}\right)^2}}{\partial z_0}=\dfrac{2k^2}{\left(a_0+u_{c0}\right)^2-\left(a_{c0}-y_0\tan\alpha\right)^2} \\ \left(\dfrac{\left(a_0{}^2-\left(a_{c0}-y_0\tan\alpha\right)^2\right)\left(a_0+u_{c0}\right)\left(1+\dfrac{\partial u_{c0}}{\partial a_0}\right)}{\left(a_0+u_{c0}\right)^2-\left(a_{c0}-y_0\tan\alpha\right)^2}-a_0\right)\dfrac{\partial a_0}{\partial z_0} \end{cases} \tag{35}$$

$$\begin{cases} \dfrac{\partial a_0}{\partial x_0}=\dfrac{x_0+a_{c0}}{a_0} \\ \dfrac{\partial a_0}{\partial z_0}=\dfrac{z_0}{k^2a_0} \end{cases} \tag{36}$$

Here, $E\left(\theta\,|\,m\right)=\int_0^\theta\sqrt{1-m^2\sin^2\beta}d\beta$ and $F\left(\theta\,|\,m\right)=\int_0^\theta\dfrac{d\beta}{\sqrt{1-m^2\sin^2\beta}}$ are incomplete elliptic integral of the second and first kind, respectively.

The arc length from *F* to *M* is expressed as

$$l_M=a_0\left[E\left(\sqrt{1-k^2}\right)-E\left(\theta_0\,|\,\sqrt{1-k^2}\right)\right] \tag{37}$$

$$\theta_0=\arcsin\left(\frac{x_0+a_{c0}}{a_0}\right) \tag{38}$$

$$\begin{cases} \dfrac{\partial\theta_0}{\partial x_0} = \dfrac{1}{\sqrt{{a_0}^2-\left(x_0+a_{c0}\right)^2}}\left(1-\dfrac{x_0+a_{c0}}{a_0}\dfrac{\partial a_0}{\partial x_0}\right) \\ \dfrac{\partial\theta_0}{\partial z_0} = \dfrac{1}{\sqrt{{a_0}^2-\left(x_0+a_{c0}\right)^2}}\left(-\dfrac{x_0+a_{c0}}{a_0}\dfrac{\partial a_0}{\partial z_0}\right) \end{cases} \tag{39}$$

$$\Delta l_M = \begin{pmatrix} \dfrac{\partial l_M}{\partial x_0} \\ \dfrac{\partial l_M}{\partial z_0} \end{pmatrix} = \begin{pmatrix} \dfrac{\partial a_0}{\partial x_0}\left[E\left(\sqrt{1-k^2}\right)-E\left(\theta_0\,|\,\sqrt{1-k^2}\right)\right]-a_0\sqrt{1-\left(1-k^2\right)\sin^2\theta_0}\,\dfrac{\partial\theta_0}{\partial x_0} \\ \dfrac{\partial a_0}{\partial z_0}\left[E\left(\sqrt{1-k^2}\right)-E\left(\theta_0\,|\,\sqrt{1-k^2}\right)\right]-a_0\sqrt{1-\left(1-k^2\right)\sin^2\theta_0}\,\dfrac{\partial\theta_0}{\partial z_0} \end{pmatrix} \tag{40}$$

The moving direction of *M* is as follow

$$\mathrm{T} = \left(\frac{-z_0}{\sqrt{{z_0}^2+k^4\left(x_0+a_{c0}\right)^2}}, \frac{x_0+a_{c0}}{\sqrt{\left(\dfrac{z_0}{k^2}\right)^2+\left(x_0+a_{c0}\right)^2}} \right)^T \tag{41}$$

$$\Delta\mathrm{T} = \begin{bmatrix} \dfrac{\partial T_x}{\partial x_0} & \dfrac{\partial T_x}{\partial z_0} \\ \dfrac{\partial T_z}{\partial x_0} & \dfrac{\partial T_z}{\partial z_0} \end{bmatrix} = \begin{bmatrix} k^2\tan\left(\dfrac{\pi}{2}-\theta_0\right) & -k^2 \\ \tan^2\left(\dfrac{\pi}{2}-\theta_0\right) & -\tan\left(\dfrac{\pi}{2}-\theta_0\right) \end{bmatrix} \frac{k^2\sqrt{\tan^2\left(\dfrac{\pi}{2}-\theta_0\right)+k^4}}{\left(x_0+a_{c0}\right)\left(\tan^2\left(\dfrac{\pi}{2}-\theta_0\right)+k^4\right)^2} \tag{42}$$

2.2.3 α=45°，parabolic section

As shown in Fig. 6, when α=45°, the section of the cone is a parabolic curve. Thus the equation of the line across $M(x_0,y_0,z_0)$ is expressed as

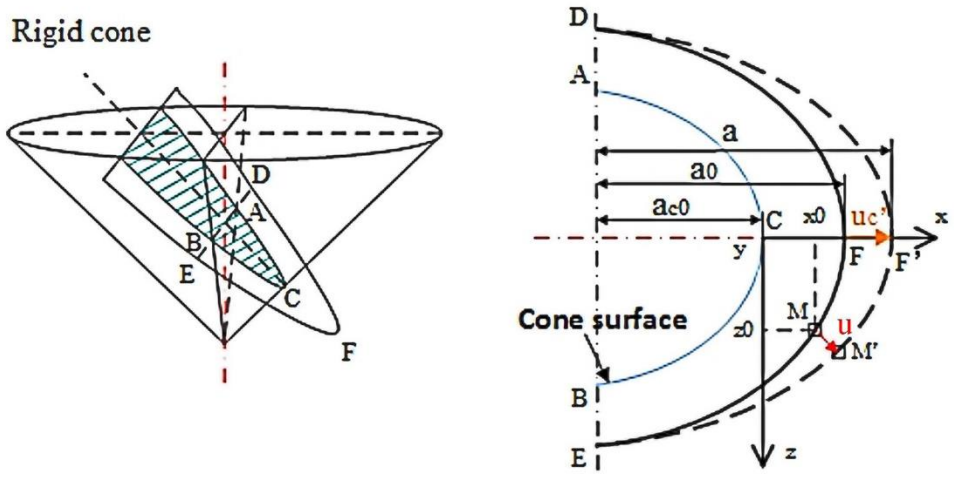

Fig. 6 *XZ* section across an arbitrary point *M* with the cone angle α=45˚.

$$x = A_0 z^2 + \left(a_0 - a_{c0}\right) \tag{43}$$

Due to the geometry assumption, a_{c0} can be expressed as:

$$a_{c0} = y_0 \tan\alpha \tag{44}$$

According to the geometric similarity, the equation of line *ACB* can be expressed as:

$$x = A_0 z^2 \tag{45}$$

Substituting the coordinate value of *C* (0, 0) and *B* $(-y_0 \tan\alpha\,, y_0 \tan\alpha \,/\, \cos\alpha)$ into Eq. (45), the following equation can be obtained:

$$A_0 = -\frac{\cos^2\alpha}{y_0 \tan\alpha} \tag{46}$$

Substituting Eq. (46) into Eq. (43) and considering point *M*, the following equation is derived:

$$a_0 = x_0 + \frac{z_0^{\,2}\cos^2\alpha}{y_0 \tan\alpha} + y_0 \tan\alpha \tag{47}$$

After deformation, curve passes point *F'* $(a_0 - a_{c0} + u_{c0}, 0)$ and *E* $(-a_{c0}, \sqrt{-\frac{a_0}{A_0}})$, thus:

$$\begin{cases} A = \left(1 + \dfrac{u_{c0}}{a_0}\right) A_0 \\ a = a_0 + u_{c0} \end{cases} \tag{48}$$

$$u_{c0} = \frac{u_c}{C_0^{\,2}}\left(a_0 - a_{c0}\right)^2 - \frac{2u_c}{C_0}\left(a_0 - a_{c0}\right) + u_c \tag{49}$$

$$\Delta u_{c0} = \begin{pmatrix} \dfrac{\partial \Delta u_{c0}}{\partial x_0} \\ \dfrac{\partial \Delta u_{c0}}{\partial z_0} \end{pmatrix} = \frac{2u_c}{C_0}\left(\frac{a_0 - a_{c0}}{C_0} - 1\right)\begin{pmatrix} 1 \\ \dfrac{2z_0 \cos^2 \alpha}{y_0 \tan \alpha} \end{pmatrix} \tag{50}$$

The elongation of the curve after deformation is:

$$\delta l = \frac{\int_0^{z_e} \sqrt{\left(2Az\right)^2 + 1}\,dz}{\int_0^{z_e} \sqrt{\left(2A_0 z\right)^2 + 1}\,dz} - 1 = \frac{A_0\left(Az_e\sqrt{\left(2Az_e\right)^2 + 1} + \dfrac{1}{2}\ln\left(2Az_e + \sqrt{\left(2Az_e\right)^2 + 1}\right)\right)}{A\left(A_0 z_e\sqrt{\left(2A_0 z_e\right)^2 + 1} + \dfrac{1}{2}\ln\left(2A_0 z_e + \sqrt{\left(2A_0 z_e\right)^2 + 1}\right)\right)} - 1 \tag{51}$$

$$z_e = \sqrt{-\frac{a_0}{A_0}} \tag{52}$$

$$\Delta\delta l = \begin{pmatrix} \dfrac{p}{qP}\left(\sqrt{q^2+1} - \dfrac{Q}{q}\right)\dfrac{\partial q}{\partial x_0} + \dfrac{Q}{qP}\left(1 - \dfrac{p\sqrt{p^2+1}}{P}\right)\dfrac{\partial p}{\partial x_0} \\ \dfrac{p}{qP}\left(\sqrt{q^2+1} - \dfrac{Q}{q}\right)\dfrac{\partial q}{\partial z_0} + \dfrac{Q}{qP}\left(1 - \dfrac{p\sqrt{p^2+1}}{P}\right)\dfrac{\partial p}{\partial z_0} \end{pmatrix} \tag{53}$$

Here, the parameters are given as:

$$
\begin{gathered}
p = 2A_0 z_e \\
q = 2Az_e \\
\frac{\partial p}{\partial x_0} = -\frac{1}{z_e} \\
\frac{\partial q}{\partial x_0} = 2A_0 z_e \left(\frac{u_c}{{C_0}^2} - \frac{u_c}{{a_0}^2} \left(\frac{a_{c0}}{C_0} + 1 \right)^2 \right) - \frac{1}{z_e} \left(\frac{u_{c0}}{a_0} + 1 \right) \\
\frac{\partial p}{\partial z_0} = -\frac{2z_0 \cos^2 \alpha}{z_e y_0 \tan \alpha} \\
\frac{\partial q}{\partial z_0} = \left(2A_0 z_e \left(\frac{u_c}{{C_0}^2} - \frac{u_c}{{a_0}^2} \left(\frac{a_{c0}}{C_0} + 1 \right)^2 \right) - \frac{1}{z_e} \left(\frac{u_{c0}}{a_0} + 1 \right) \right) \frac{2z_0 \cos^2 \alpha}{y_0 \tan \alpha} \\
P = \frac{p}{2} \sqrt{p^2 + 1} + \frac{1}{2} \ln \left(p + \sqrt{p^2 + 1} \right) \\
Q = \frac{q}{2} \sqrt{q^2 + 1} + \frac{1}{2} \ln \left(q + \sqrt{q^2 + 1} \right)
\end{gathered}
\tag{54}
$$

The arc length from *F* to *M* can be expressed as:

$$
l_M = \frac{1}{2A_0} \left(A_0 z_0 \sqrt{\left(2A_0 z_0 \right)^2 + 1} + \frac{1}{2} \ln \left(2A_0 z_0 + \sqrt{\left(2A_0 z_0 \right)^2 + 1} \right) \right) \tag{55}
$$

$$
\Delta l_M = \begin{pmatrix} 0 \\ 2A_0 \sqrt{\left(2A_0 z_0 \right)^2 + 1} \end{pmatrix} \tag{56}
$$

The moving direction of *M* is as follow:

$$
T = \begin{pmatrix} \dfrac{1}{\sqrt{\left(2A_0 z_0 \right)^2 + 1}} \\ \dfrac{2A_0 z_0}{\sqrt{\left(2A_0 z_0 \right)^2 + 1}} \end{pmatrix} \tag{57}
$$

$$\Delta T = \begin{bmatrix} \frac{\partial T_x}{\partial x_0} & \frac{\partial T_x}{\partial z_0} \\ \frac{\partial T_z}{\partial x_0} & \frac{\partial T_z}{\partial z_0} \end{bmatrix} = \begin{bmatrix} 0 & -\frac{4A_0^2 z_0 \sqrt{(2A_0 z_0)^2 + 1}}{\left[(2A_0 z_0)^2 + 1\right]^2} \\ 0 & \frac{2A_0 \sqrt{(2A_0 z_0)^2 + 1}}{\left[(2A_0 z_0)^2 + 1\right]^2} \end{bmatrix} \tag{58}$$

2.2.4 α>45˚ hyperbolic section

As shown in Fig. 7, when α>45˚, the section of the cone is a hyperbolic curve. Thus the equation of the line across $M(x_0,y_0,z_0)$ is expressed as:

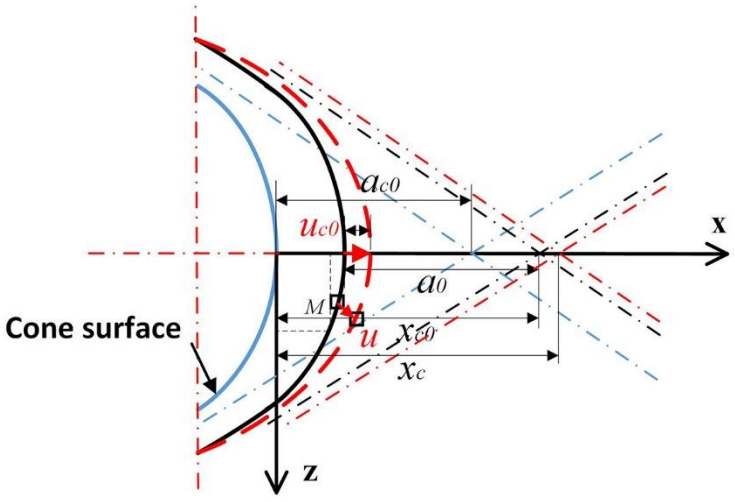

Fig. 7 *XZ* section across an arbitrary point *M* with the semi cone angle α>45˚.

$$\left(\frac{x - x_{c0}}{a_0}\right)^2 - \left(\frac{z}{b_0}\right)^2 = 1 \tag{59}$$

The equation of *ACB* is expressed as

$$\left(\frac{x - a_{c0}}{a_{c0}}\right)^2 - \left(\frac{z}{b_{c0}}\right)^2 = 1 \tag{60}$$

Due to the geometry, a_{c0} is expressed as

$$a_{c0} = -\frac{y_0 \tan 2\alpha}{2} \tag{61}$$

As curve *ACB* passes point $B\left(-y_0 \tan\alpha, \frac{y_0 \tan\alpha}{\cos\alpha}\right)$, b_{c0} is thus obtained based on Eq. (61).

$$b_{c0} = \frac{y_0 \tan\alpha}{\sqrt{\tan^2\alpha - 1}} \tag{62}$$

As curve *DFE* is similar to *ACB*, the following equation is obtained:

$$\begin{cases} a_0 = a_{c0} \\ b_0 = b_{c0} \end{cases} \tag{63}$$

By substituting Eqs. (61)~(63) and point *M* into Eq. (59), the following equation is obtained:

$$x_{c0} = \sqrt{{a_{c0}}^2 + \left(\frac{z_0}{k}\right)^2} + x_0 \tag{64}$$

$$k = \frac{b_{c0}}{a_{c0}} = \sqrt{\tan^2\alpha - 1} \tag{65}$$

The arc length from *F* to *M* is expressed as:

$$l_M = \int_0^{z_0} \sqrt{1 + \frac{1}{k^2} - \frac{{a_{c0}}^2}{z^2 + \left(k a_{c0}\right)^2}}\, dz \tag{66}$$

$$\Delta l_M = \begin{pmatrix} \frac{\partial l_M}{\partial x_0} \\ \frac{\partial l_M}{\partial z_0} \end{pmatrix} = \begin{pmatrix} 0 \\ \sqrt{1 + \frac{1}{k^2} - \frac{{a_{c0}}^2}{{z_0}^2 + \left(k a_{c0}\right)^2}} \end{pmatrix} \tag{67}$$

Considering that both compress and sliding don't change the value of *k*, the equation of *DF'E* is assumed as

$$\left(\frac{x - x_c}{a}\right)^2 - \left(\frac{z}{ka}\right)^2 = 1 \tag{68}$$

Substituting point F' $(x_{c0} - a_{c0} + u_{c0}, 0)$ and E $\left(-y_0 \tan\alpha, k\sqrt{\left(y_0 \tan\alpha + x_{c0}\right)^2 - {a_{c0}}^2}\right)$ into Eq. (68), the following equation is obtained:

$$\begin{cases} a = \dfrac{2\left(y_0 \tan\alpha + x_{c0}\right)\left(a_{c0} - u_{c0}\right) - {a_{c0}}^2 - \left(a_{c0} - u_{c0}\right)^2}{2\left(y_0 \tan\alpha + x_{c0} - a_{c0} + u_{c0}\right)} \\ x_c = a - a_{c0} + x_{c0} + u_{c0} \end{cases} \tag{69}$$

The elongation of the curve is deduced as

$$\delta l = \frac{\int_0^{z_e} \sqrt{1 + \dfrac{1}{k^2} - \dfrac{a^2}{z^2 + \left(ka\right)^2}}\, dz}{\int_0^{z_e} \sqrt{1 + \dfrac{1}{k^2} - \dfrac{{a_0}^2}{z^2 + \left(ka_0\right)^2}}\, dz} - 1 \tag{70}$$

By making $H(z_e, a) = \int_0^{z_e} \sqrt{1 + \dfrac{1}{k^2} - \dfrac{a^2}{z^2 + \left(ka\right)^2}}\, dz$, and $z_e = k\sqrt{\left(y_0 \tan\alpha + x_{c0}\right)^2 - {a_{c0}}^2}$, the following equations can be obtained according to the partial derivation of compound functions:

$$\begin{cases} \dfrac{\partial H}{\partial x_0} = \dfrac{\partial H}{\partial z_e}\dfrac{\partial z_e}{\partial x_0} + \dfrac{\partial H}{\partial a}\dfrac{\partial a}{\partial x_0} \\ \dfrac{\partial H}{\partial z_0} = \dfrac{\partial H}{\partial z_e}\dfrac{\partial z_e}{\partial z_0} + \dfrac{\partial H}{\partial a}\dfrac{\partial a}{\partial z_0} \end{cases} \tag{71}$$

$$\frac{\partial H}{\partial z_e} = \sqrt{1 + \frac{1}{k^2} - \frac{a^2}{{z_e}^2 + \left(ka\right)^2}} \tag{72}$$

Based on the law of mixed partial derivation, $\frac{\partial H}{\partial a}$ is obtained as follows:

$$\begin{aligned} \frac{\partial H}{\partial a} &= \int \frac{\partial^2 H}{\partial a \partial z_e} dz_e = \int \frac{\partial}{\partial a}\left(\frac{\partial H}{\partial z_e}\right) dz_e = \int \frac{-a{z_e}^2}{\sqrt{1 + \dfrac{1}{k^2} - \dfrac{a^2}{{z_e}^2 + \left(ka\right)^2}}\left({z_e}^2 + \left(ka\right)^2\right)^2} dz_e \\ &= -\frac{z_e}{a}\sqrt{1 + \frac{1}{k^2} - \frac{a^2}{{z_e}^2 + \left(ka\right)^2}} + \frac{1}{a}\int_0^{z_e} \sqrt{1 + \frac{1}{k^2} - \frac{a^2}{z^2 + \left(ka\right)^2}} dz \end{aligned} \tag{73}$$

The gradient of elongation is expressed as:

$$\Delta\delta l = \begin{pmatrix} \dfrac{1}{H(z_e,a_0)}\left(\dfrac{\partial H(z_e,a)}{\partial z_e}\dfrac{\partial z_e}{\partial x_0}+\dfrac{\partial H(z_e,a)}{\partial a}\dfrac{\partial a}{\partial x_0}\right) \\ -\dfrac{H(z_e,a)}{H(z_e,a_0)}\dfrac{\partial H(z_e,a_0)}{\partial z_e}\dfrac{\partial z_e}{\partial x_0} \\ \dfrac{1}{H(z_e,a_0)}\left(\dfrac{\partial H(z_e,a)}{\partial z_e}\dfrac{\partial z_e}{\partial z_0}+\dfrac{\partial H(z_e,a)}{\partial a}\dfrac{\partial a}{\partial z_0}\right) \\ -\dfrac{H(z_e,a)}{H(z_e,a_0)}\dfrac{\partial H(z_e,a_0)}{\partial z_e}\dfrac{\partial z_e}{\partial z_0} \end{pmatrix} \tag{74}$$

$$\begin{cases} \dfrac{\partial z_e}{\partial x_0}=\dfrac{k(y_0\tan\alpha+x_{c0})}{\sqrt{(y_0\tan\alpha+x_{c0})^2-{a_{c0}}^2}}\dfrac{\partial x_{c0}}{\partial x_0} \\ \dfrac{\partial z_e}{\partial z_0}=\dfrac{k(y_0\tan\alpha+x_{c0})}{\sqrt{(y_0\tan\alpha+x_{c0})^2-{a_{c0}}^2}}\dfrac{\partial x_{c0}}{\partial z_0} \\ \dfrac{\partial a}{\partial x_0}=\dfrac{{a_{c0}}^2-(a_{c0}-u_{c0})^2}{2(y_0\tan\alpha+x_{c0}-a_{c0}+u_{c0})}\left(\dfrac{\partial x_{c0}}{\partial x_0}+\dfrac{\partial u_{c0}}{\partial x_0}\right) \\ +\left(\dfrac{a_{c0}-u_{c0}}{y_0\tan\alpha+x_{c0}-a_{c0}+u_{c0}}-1\right)\dfrac{\partial u_{c0}}{\partial x_0} \\ \dfrac{\partial a}{\partial z_0}=\dfrac{{a_{c0}}^2-(a_{c0}-u_{c0})^2}{2(y_0\tan\alpha+x_{c0}-a_{c0}+u_{c0})}\left(\dfrac{\partial x_{c0}}{\partial z_0}+\dfrac{\partial u_{c0}}{\partial z_0}\right) \\ +\left(\dfrac{a_{c0}-u_{c0}}{y_0\tan\alpha+x_{c0}-a_{c0}+u_{c0}}-1\right)\dfrac{\partial u_{c0}}{\partial z_0} \end{cases} \tag{75}$$

$$u_{c0}=\frac{u_c}{{C_0}^2}(x_{c0}-a_{c0})^2-\frac{2u_c}{C_0}(x_{c0}-a_{c0})+u_c \tag{76}$$

$$\begin{cases} \dfrac{\partial u_{c0}}{\partial x_0} = \dfrac{2u_c\left(x_{c0}-a_{c0}-C_0\right)}{{C_0}^2}\dfrac{\partial x_{c0}}{\partial x_0} \\ \dfrac{\partial u_{c0}}{\partial z_0} = \dfrac{2u_c\left(x_{c0}-a_{c0}-C_0\right)}{{C_0}^2}\dfrac{\partial x_{c0}}{\partial z_0} \\ \dfrac{\partial x_{c0}}{\partial x_0} = 1 \\ \dfrac{\partial x_{c0}}{\partial z_0} = \dfrac{2z_0}{k^2\sqrt{{a_{c0}}^2+\left(\dfrac{z_0}{k}\right)^2}} \end{cases} \tag{77}$$

The traveling direction of *M* can be expressed as follows:

$$\mathrm{T} = \left(\frac{-z_0}{\sqrt{{z_0}^2+k^4\left(x_0-x_{c0}\right)^2}}, \frac{-k^2\left(x_0-x_{c0}\right)}{\sqrt{{z_0}^2+k^4\left(x_0-x_{c0}\right)^2}} \right)^T \tag{78}$$

$$\Delta T = \begin{bmatrix} \dfrac{\partial T_x}{\partial x_0} & \dfrac{\partial T_x}{\partial z_0} \\ \dfrac{\partial T_z}{\partial x_0} & \dfrac{\partial T_z}{\partial z_0} \end{bmatrix} = \begin{bmatrix} 0 & \dfrac{-k^4{a_{c0}}^2}{\left(\left(1+k^2\right){z_0}^2+k^4{a_{c0}}^2\right)^{\frac{3}{2}}} \\ 0 & \dfrac{k^3{a_{c0}}^2 z_0}{\sqrt{k^2{a_{c0}}^2+{z_0}^2}\left(\left(1+k^2\right){z_0}^2+k^4{a_{c0}}^2\right)^{\frac{3}{2}}} \end{bmatrix} \tag{79}$$

2.3 Strain increment considering the bulge effect

According to the volume constancy, the compression of material leads to the bulging on the free surface. Hence the evident pile-up of materials in front of the indenter can be observed in the scratching process. To model the bulging effect, the pile-up is regarded as the increase of *Y* coordinate value of the mass points in the *XYZ* coordinate system, which is an extension load to the line element as shown in Fig. 8. The line element is assumed to be concentric elliptical with the cone surface.

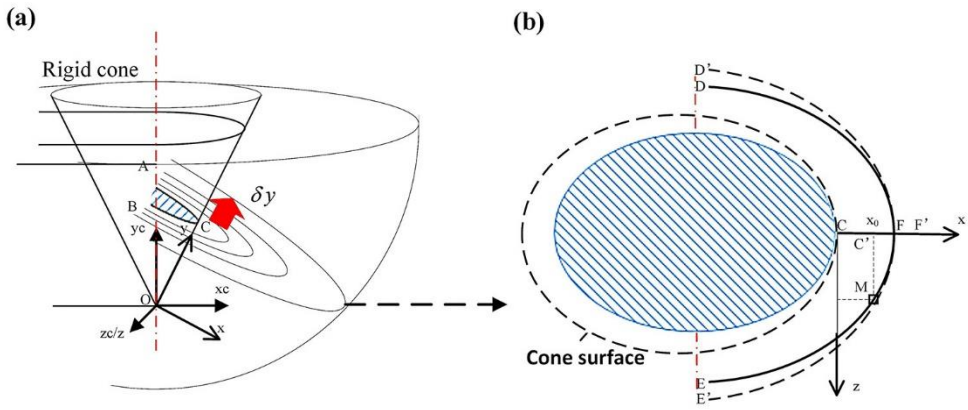

Fig. 8 Strain increment caused by the bulging effect.

Given a small increment δy in the Y direction of one point C, the cone intersection line corresponding to the point changes from the solid line to the dashed line as shown in Fig. 8 (b). Similarly, the line element that crosses M changes from DFE to $D'F'E'$. According to the assumption of uniform elongation, the elongation ratio of M can be expressed as follow:

$$\delta l = \frac{l_{D'F'E'}}{l_{DFE}} - 1 \tag{80}$$

According to Eqs. (61) and (66), l_{DFE} and $l_{D'F'E'}$ can be calculated as:

$$\begin{cases} l_{DFE} = 2\int_0^{z_i} \sqrt{1 + \dfrac{1}{k^2} - \dfrac{a_{ci}^{\,2}}{z^2 + \left(k a_{ci}\right)^2}}\, dz \\ a_{ci} = -\dfrac{y_0 \tan 2\alpha}{2} \\ z_i = k\sqrt{\left(y_0 \tan\alpha + x_{ci}\right)^2 - a_{ci}^{\,2}} \\ x_{ci} = \sqrt{a_{ci}^{\,2} + \left(\dfrac{z_0}{k}\right)^2} + x_0 \end{cases} \tag{81}$$

$$\begin{cases} l_{D'F'E'} = 2\int_0^{z_r} \sqrt{1+\dfrac{1}{k^2}-\dfrac{a_{cr}{}^2}{z^2+\left(ka_{cr}\right)^2}}dz \\ a_{cr} = -\dfrac{\left(y_0+\delta y\right)\tan 2\alpha}{2} \\ z_r = k\sqrt{\left(\left(y_0+\delta y\right)\tan\alpha + x_{cr}\right)^2 - a_{cr}{}^2} \\ x_{cr} = \sqrt{a_{cr}{}^2+\left(\dfrac{z_0}{k}\right)^2} + x_0 \end{cases} \tag{82}$$

Here, x_0,y_0,z_0 are the coordinate values of *M*.

Assuming the increase of height do not affect the strain in *Y* direction, the strain caused by the increase of height in the symmetry section can be obtained

$$\varepsilon = \begin{bmatrix} -\ln\left(\delta l+1\right) & 0 & 0 \\ 0 & 0 & 0 \\ 0 & 0 & \ln\left(\delta l+1\right) \end{bmatrix} \tag{83}$$

As δy is caused by the compression barreling, it can be calculated based on the following equation:

$$\delta y = \int_{y_r}^{y_0} \left(1+\varepsilon_y\right) dy \tag{84}$$

Here, y_r is the *Y* coordinate value of cone tip, and ε_y is the strain in *Y* direction.

2.4 Calculation procedure and numerical results

2.4.1 Matlab procedure

An iteration approach was developed with the help of MATLAB to calculate the strain field of the symmetry section (with $z=0$) at the front edge of rigid cone. The flow chart of the solution is shown in Fig. 9. During the calculation, the displacement of rigid tool is discretized into incremental steps. The strain increment caused by the scratching and bulging effects are then calculated using Eqs.

(15)-(21) for each local calculation node. Depending on the cone angle level, the moving direction and length for each node can also be calculated according to Eqs. (40-42), (55-57) and (67,78, 79). The strain and coordinates of each point are updated upon each increment. Once the mass point flows over the rigid tool, its strain is no longer recorded, and the new points that flow into the deformation region are further computed. The strain field calculation for the scratching process is determined by 6 parameters, namely the semi-angle of the cone α, the Young's modulus E, yielding stress Y and Poisson's modulus ν of the material, the indented depth hp and the scratch distance uc. However, the adhesion on the tool-workpiece interface and the strain hardening of material is ignored in this research.

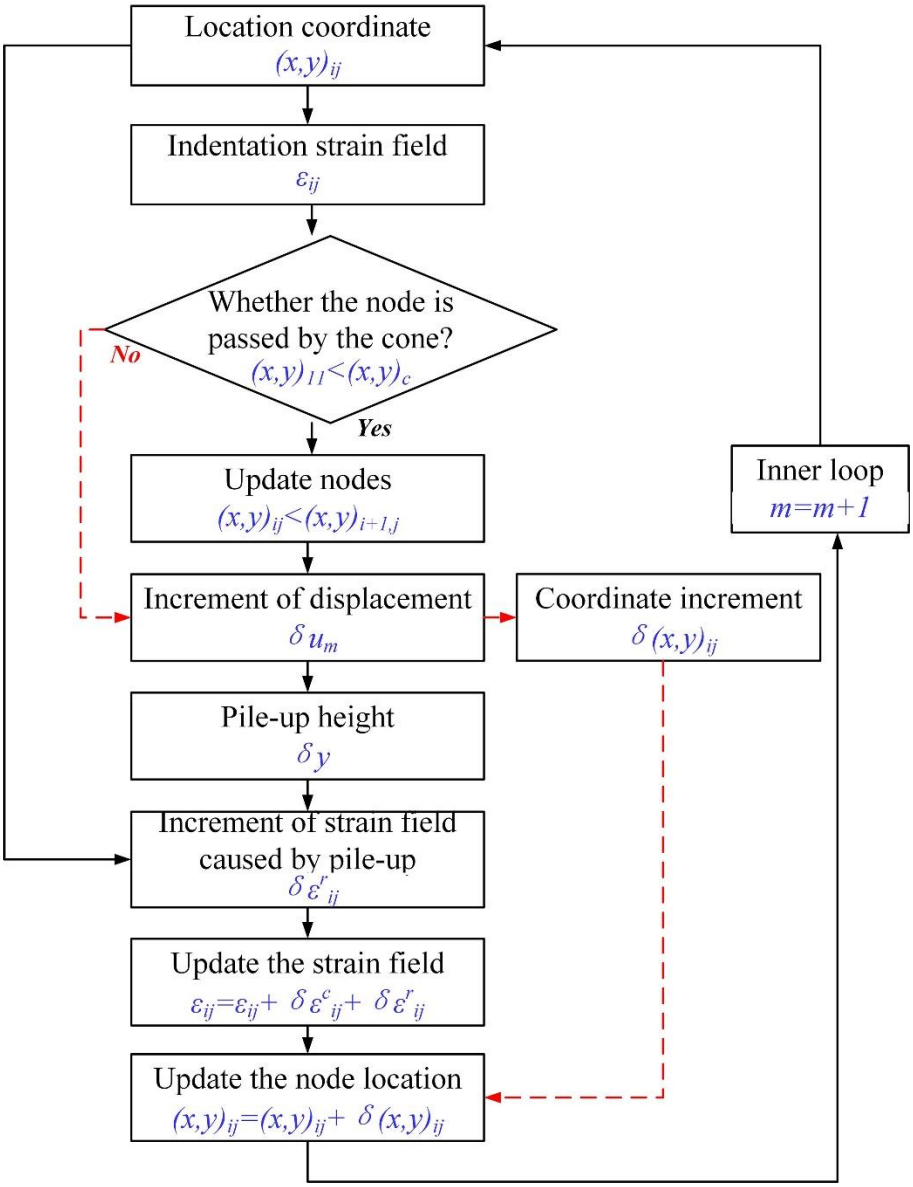

Fig. 9 The calculation procedure.

2.4.2 Strain field in scratching process

To verify the calculation procedure, a comparison was made between the numerical results obtained based on the developed model and the FE simulation. The input parameters are listed in Table 1:

Table 1 The specified values of parameters values in the verification FE and analytical models.

Parameters	Values (FE/Analytical model)
Young's modulus E	100 GPa
Poisson ratio v	0.495
Cone angle α	120°
Yield stress Y	400MPa
Indented depth h_p	0.1 mm
Scratch distance u_c	0.5 mm

Furthermore, the three-dimensional FE models were constructed in ABAQUS/Standard environment. The scratch direction was along x axis. Only half of the system was used to do simulation and a symmetric plane was defined to minimize the computation scale, as shown in Fig.10.

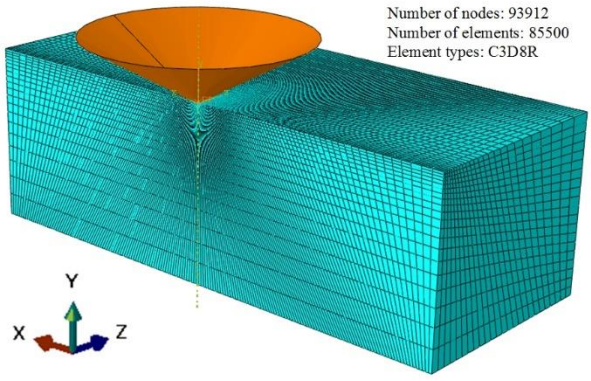

Fig. 10 The scratching simulation model.

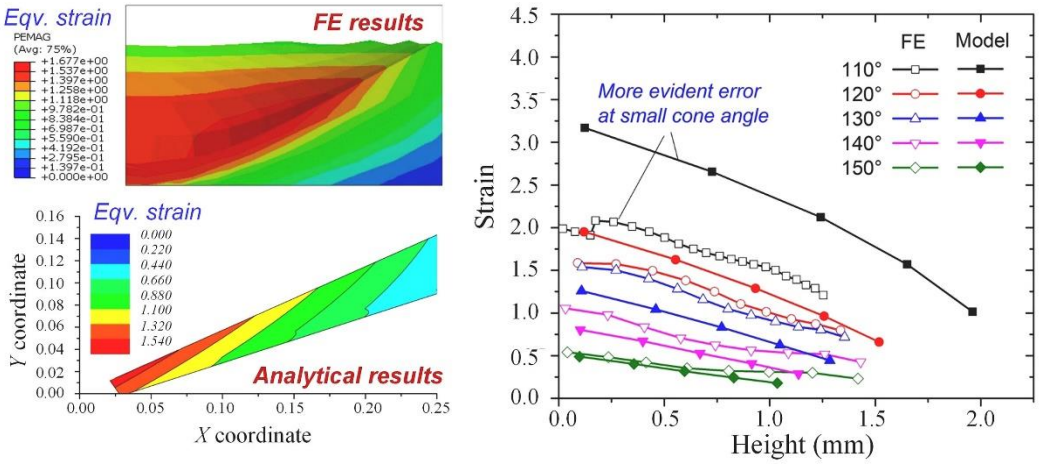

Fig. 11 Strain distribution results obtained based on FE simulation and the presented analytical model.

Fig. 11 presents the comparison of the evolutions of equivalent strain in symmetry section of the leading ridge with the increase of scratch distance predicted by the FE simulations and the developed analytical model. A satisfactory agreement of strain field distribution is observed between the simulation and analytical results. In addition, both methods reveal that the equivalent strain at different positions is increased with the decrease of the cone angle. The maximum equivalent strain appears at the cone tip and decreases with the increase of height. The predicted height-strain curves based on the analytical model, however, are higher than the FE results with the small cone angle of 110°. This is because the existence of element distortion is observed in the simulations with the cone angle of 110°, leading to the underestimation of strain level. On the other hand, the distortion did not exist in the FE simulations with the larger cone angles (120° and above) since the strain condition is less severe. In comparison, the element distortion problem does not exist in the analytical model. Deviation is thus expected between FE and analytical results. Further research addressing the element distortion problem in FE models need to be conducted in future

to verify the model in the cases with smaller cone angles. In this work, an experimental validation with the cone angle of 45° is presented in Section 3.

The FE results also indicate a proper analytical description of the fracture mechanisms in the scratching process could be more applicable than simulations in engineering problems. In addition to the calculation efficiency, the analytical model could also be easily incorporated into machine learning frameworks for different engineering applications. The idea has been attracting a lot of attentions with the fast development of computation and artificial intelligent technologies. Application examples have been reported on small fatigue cracks in polycrystalline materials [33], fracture of DP steel under elevated temperatures [34], dynamic fracture growth in brittle materials [35], Strain rate and temperature dependent fracture [36], etc. Therefore, the analytical method developed in this work is useful to handle the ploughing effects in various machining and forming processes by combining with machine learning in future study.

2.4.3 Pile up ratio in the stable state of scratching process

The pile up ratio of leading edge in stable state is defined as the ratio of the pile up height to the indented depth, which is an important parameter affecting the total scratching resistance. It can also be predicted based on the calculated strain field. As the adhesive effect on the deformation of material is ignored, the maximum pile up ratio occurs at the interface of the contact, where the maximum y-strain is generated. According to the definition, the pile up ratio of leading edge is expressed as follows:

$$r_{pileup} = \frac{h_{pileup}}{h_{indent}} = \frac{\int_{ry_h}^{y_h} \varepsilon_y dy}{y_h (1-r)} \tag{85}$$

Here, r_{pileup} and h_{pileup} are the pile up ratio and height of leading edge, respectively. And h_{indent} represents the initial indented depth. y_h is the *y* coordinate value of the leading edge in *XYZ* system, and *r* is the ratio that the tip radius takes in the total indented depth. Notably, the tip radius is not considered in the model. Hence the strain in the tip radius part is not included in the calculation. According to the developed analytical model, the distribution of strain in the front ridge is determined as follows:

$$\boldsymbol{\varepsilon} = \boldsymbol{\varepsilon}_t + \int_y^{y_h(1+r_{pileup})} \frac{\partial \delta \boldsymbol{\varepsilon}}{\partial \delta u} dy \tag{86}$$

Here, $\delta\boldsymbol{\varepsilon} = \delta\boldsymbol{\varepsilon}^c + \delta\boldsymbol{\varepsilon}^r$ is the strain increment with a small tool displacement of δu given by Eqs. (15)-(19). Thus the above equation can be further derived. $\boldsymbol{\varepsilon}_t$ represents the initial strain of a new point that flow into the iteration, which is given by Eq. (83) with $\delta y = r y_h$. At the stable state, the pile up height does not increase with the scratch distance. Therefore, *r* is independent of δu. In addition, according to Eq. (85), the pileup ratio is affected by ε_y. By substituting Eqs.(18) and (83) into Eq. (86), the following equation is deduced:

$$\varepsilon_y(y) = \int_y^{y_h(1+r)} \frac{\partial \delta \varepsilon_y^{\,c}}{\partial \delta u} dy \tag{87}$$

According to Eqs. (59) to (79) and (18), Eq.(85) can be rewritten as the following equation by making *z=0*:

$$y_h\left(1+r_{pileup}\right) r_{pileup} = \int_{r y_h}^{y_h} \int_y^{y_h\left(1+r_{pileup}\right)} \left[\begin{array}{l} \dfrac{1}{2}\left(1 - \dfrac{kt\sqrt{(\tan\alpha - \tan 2\alpha)\tan\alpha}}{\int_0^{kt\sqrt{(\tan\alpha-\tan 2\alpha)\tan\alpha}} \sqrt{1+\dfrac{1}{k^2} - \dfrac{t^2 \tan 2\alpha^2}{4z^2 + k^2 t^2 \tan 2\alpha^2}}\, dz} \right) \\ (1 + t\tan\alpha - t\tan 2\alpha) + \dfrac{2}{\sqrt{C^2 - \left(t - h_p \cos\alpha\right)^2} - h_p \sin\alpha} \end{array} \right] dt dy \tag{88}$$

By making the cone angle α, the ratio of tip radius to indented depth r, and the ratio of yielding stress to Young's modulus Y/E as known parameters, the pile up ratios can be computed by solving Eq. (88) and the results are presented in Fig. 12.

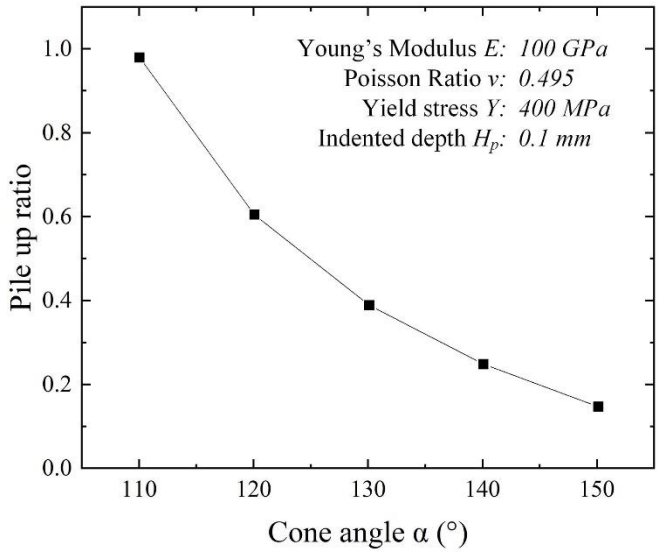

(a)

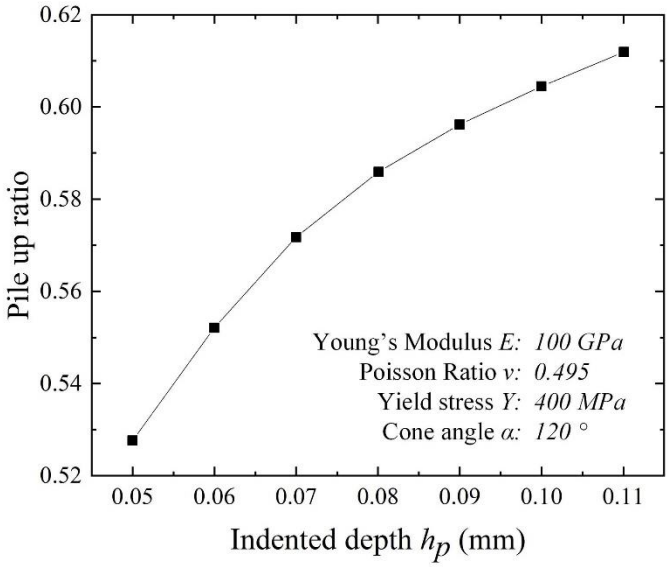

(b)

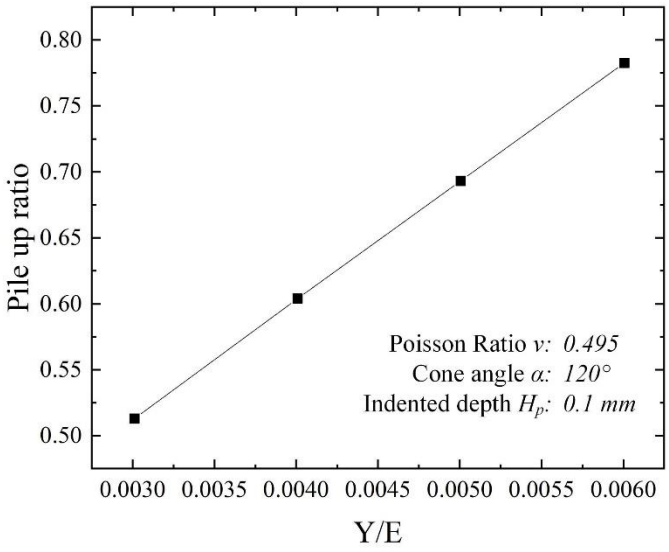

(c)

Fig. 12 The pile up ratio r_{pileup} as a function of (a) the cone angle α, (b) the ratio of tip radius to indented depth h_p, and (c) the ratio of yielding stress to young's modulus *Y/E*.

As shown in Fig. 12, the pile up height increases with the decrease of α and *r* and the increase of *Y/E*. It should be noted that the effect of *Y/E* on the pileup ratio seems not to be in accordance with the prior FE studies given by Bucaille et al. [22, 37]. They pointed out the pileup ratio increases with the rheological factor $X=E\cot\alpha/Y$. This is attributed to the different application scenarios of the two studies. In the studies of Bucaille et al., the effect of elastic recovery is considered and the transformation of elastic deformation to plastic deformation is the major mechanism of the influence of rheological factor. On the other hand, the elastic deformation is neglected in the present work, which focuses on the plastic deformation of base material.

2.4.4 Fracture in the scratching process

According to the Oyane ductile fracture criterion [38], the fracture of ductile material can be described as follows:

$$C = \int_0^{\bar{\varepsilon}_f} \left(\frac{\sigma_m}{\bar{\sigma}} + C_1 \right) d\bar{\varepsilon} \tag{89}$$

Here, σ_m is the hydrostatic stress, $\bar{\sigma}$ is the equivalent stress, $\bar{\varepsilon}_f$ is the equivalent strain at fracture. C and C_1 are material constants. As illustrated in Fig. 11, the dangerous area onset of fracture is the interface of the workpiece and the tool. For simplification, a small unit in the thin surface layer at the interface is taken as the concern of interest, assuming its deformation satisfies the plane stress condition and the Mises yield criterion, the following equation can be obtained:

$$\frac{\sigma_m}{\bar{\sigma}} = \frac{\sqrt{2}\left(\sigma_1 + \sigma_2\right)}{3\sqrt{\left(\sigma_1 - \sigma_2\right)^2 + \sigma_1^{\,2} + \sigma_2^{\,2}}} \tag{90}$$

where σ_1 and σ_2 are the major and minor principal stresses, respectively. Assuming that the load path in deformation is fixed and the elastic part can be neglected, the Levy-Mises flow rule can be given as

$$\begin{cases} \dfrac{\left(-k-1\right)\dot{\varepsilon}_2}{\sigma_1 - \sigma_2} = \dfrac{\left(1-2k\right)\dot{\varepsilon}_2}{\sigma_1} = \dfrac{\left(2-k\right)\dot{\varepsilon}_2}{\sigma_2} \\ k = -\dfrac{\dot{\varepsilon}_1}{\dot{\varepsilon}_2}, k \geq 2 \end{cases} \tag{91}$$

Here, $\dot{\varepsilon}_1$ and $\dot{\varepsilon}_2$ are the major and minor principal strain rates, respectively. The following equation can thus be obtained by substituting Eq. (91) into Eq. (90):

$$\begin{cases} \dfrac{\sigma_m}{\bar{\sigma}} = \dfrac{k-1}{\sqrt{3\left(k^2 - k + 1\right)}} \\ k \geq 2 \end{cases} \tag{92}$$

By substituting Eq. (92) into Eq. (89), the following equation is derived

$$\bar{\varepsilon}_f = \frac{C}{(k-1)/\sqrt{3\left(k^2-k+1\right)}+C_1} \tag{93}$$

In the deformed material, fracture occurs where the strain is greater than the fracture strain given by Eq. (93). Particularly, the fracture strain is not a material constant but is affected by the strain condition, which is represented by k in Eq. (93). Based on the developed model, the distributions of k and fracture strain $\bar{\varepsilon}_f$ are calculated and presented in Fig. 13. Obviously, the value of k is higher in the upper region of the front ridge than in the bottom region. Thus the fracture strain in the bottom region is higher than in the upper region. Moreover, recalling Fig. 11, the strain in the front ridge is also close to the fracture strain. It makes the occurrence of the fracture more interesting, since both the bottom and upper region in the front ridge are possible to fracture.

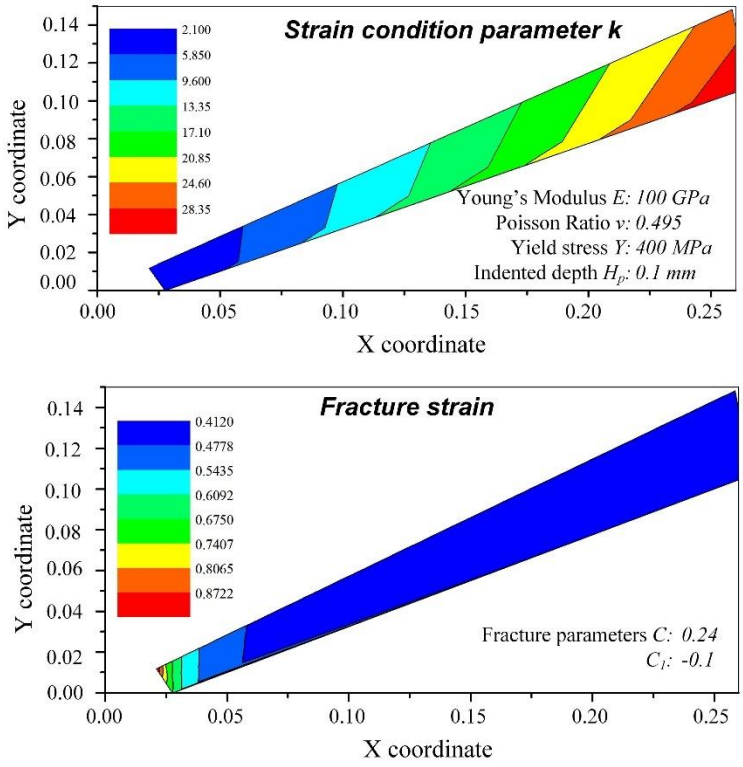

Fig. 13 Distribution of the strain condition parameter k, and the fracture strain $\bar{\varepsilon}_f$.

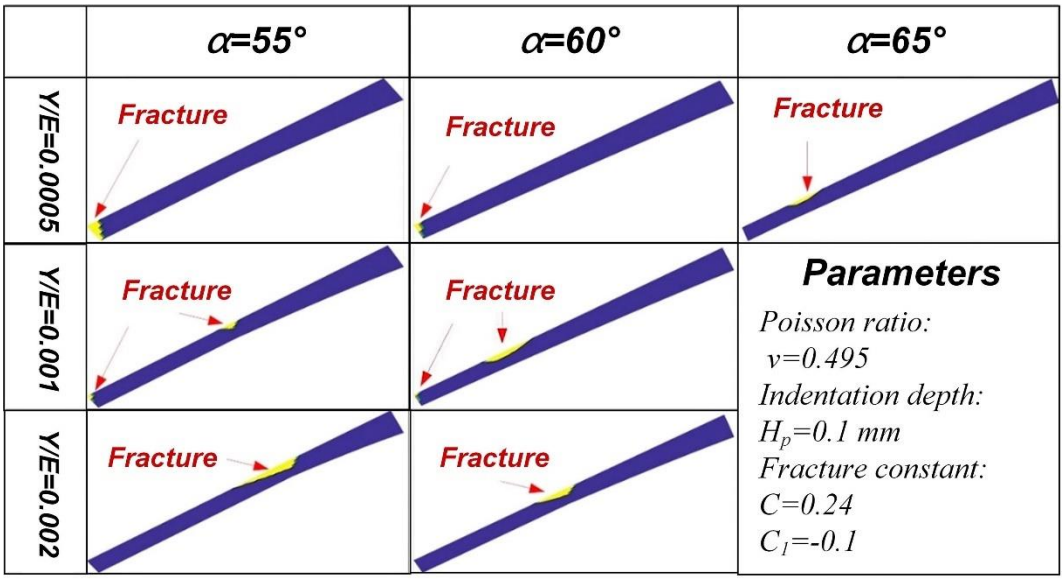

Fig. 14 The initiation of fracture in the front ridge.

Fig. 14 shows the initiation location of fracture (in yellow) in the front ridge of scratch trajectory with different semi-cone-angle α and different material property *Y/E* which was predicted by comparing the strain and the fracture strain calculated by utilizing the developed analytical model and Eq. (93) respectively. The fracture is revealed to be most likely to initiate at two locations, viz. the bottom and the middle regions of the leading edge. In the view of strain rate condition, the fractures behaviors at these two locations are different. For the fracture at the bottom of the ridge, the major and minor principal strain rate are $\dot{\varepsilon}_x$ and $\dot{\varepsilon}_z$, respectively. The value of *k* in Eq. (92) equals to $\dot{\varepsilon}_x/\dot{\varepsilon}_z$. However, for the fracture at the middle region of the ridge, the major and minor principal strain rates are $\dot{\varepsilon}_x$ and $\dot{\varepsilon}_y$ respectively. In addition, *k* is close to 2 at the bottom region, indicating that the region is under three dimensional stress condition. While *k* is much greater than 2 at the middle region which is under plane stress condition. Under three dimensional stress condition, the fracture is caused by the maximum shear stress [39, 40]. Thus it is believed the fracture initiates at the bottom of the ridge is mainly caused by the maximum shear stress, and the

crack may propagate upwards and lead to the detachment of materials. That mechanism has been well reported by many prior studies [21, 41, 42]. On the other hand, the fracture at the middle region of the ridge has not been widely reported yet. According to the stress condition, it can be attributed to the split flow of materials in front of the rigid cone, since in the upper boundary model of scratching, a velocity discontinuity is assumed in front of the indenter to simulate the split flow of materials.

According to the calculated results, the initiation location of fracture changes from bottom to middle with the increase of cone angle and *Y/E*. If the cone angle and *Y/E* further increases, the generation of fracture gradually disappears during the scratching process. This trend could be the explanation for the different scratching types observed in the experiments. As mentioned in the literature review, three different types of scratching process, which are cutting, wear and rubbing, can be observed with the decrease of attack angle. If the fracture initiates at the bottom of the ridge, the crack propagates upwards leading to the detachment of chips. Hence cutting is observed during the scratching process. If the fracture initiates in the middle of contact surface, the base material near the fracture spot flows upward and downward respectively. Due to the continuous pressure loading, no detachment of material occurs leading to the wear mode in the scratching process. Furthermore, if no fracture initiates during the process, the material flows downwards and climbs over the indenter leading to the rubbing mode.

3 Single cone scratch experiments

In order to validate the developed model, the scratching tests with different cone angles were conducted by using the copper samples with different grain sizes.

3.1 Material preparation

Copper pillars with three different grain sizes were prepared by the vacuum heat treatment to investigate the grain size effect on the friction behavior. The microstructures and grain sizes has been presented in the previous research [43, 44]. The surface hardness and elastic modulus were measured via micro-hardness and nano-indentation tests respectively. Electrochemical polishing was conducted to avoid surface hardening of the samples. The mechanical and surface properties of samples are listed in Table 2. The surface hardness is revealed to decrease with the increase of grain size. On the other hand, the elastic modulus and surface roughness are almost the same for the samples with different grain sizes.

Table 2 Mechanical and surface properties of specimen

Samples	Grain size	Surface hardness	Elastic modulus	Surface roughness
As-received	-	1182.2MPa	118.2GPa	0.026±0.005
Fine grain	4μm	745.1MPa	99.4GPa	0.027±0.007
Medium grain	12μm	507.8MPa	99.8GPa	0.026±0.008
Coarse grain	130μm	464.4MPa	99.8GPa	0.025±0.004

3.2 Scratching apparatus and measurement

The scratching apparatus is presented in Fig. 15. Both the rigid cone and the sample are positioned by using the designed holders. The rigid cone holder was connected to a load cell which was fixed on the beam of a tensile machine. Meanwhile the sample holder was fixed with the substrate of the machine. The test was divided into two steps, namely indentation and scratching. In the first step,

the holders of the rigid tool and the sample were clamped together by screw bolt so that the rigid tool can indent into the deformable surface. In the second step, the beam moved upwards to make the rigid tool scratch on the deformable surface, and the scratch force is recorded by the load cell. During the process the indent depth was kept constant. Three cone angle levels are employed in the experiments, which are 45°, 60° and 75°. The radius of the cone tip was 0.04 μm. During the scratching test, an indentation depth of 0.1 mm was first reached. After that the scratching force was applied by the load cell with a speed of 1 mm/min. Subsequently all the tested surfaces were scanned by utilizing a laser confocal scanning microscope. A typical 3D profile of the scratching trajectory is shown in Fig. 16. Two sections of A and B were employed to measure the pile-up height and projected contact area respectively.

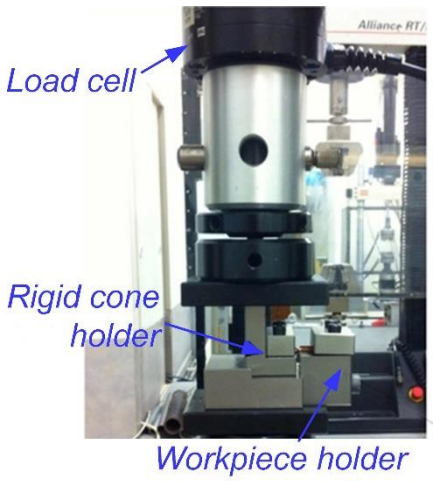

Fig. 15 Experimental apparatus of the scratching tests.

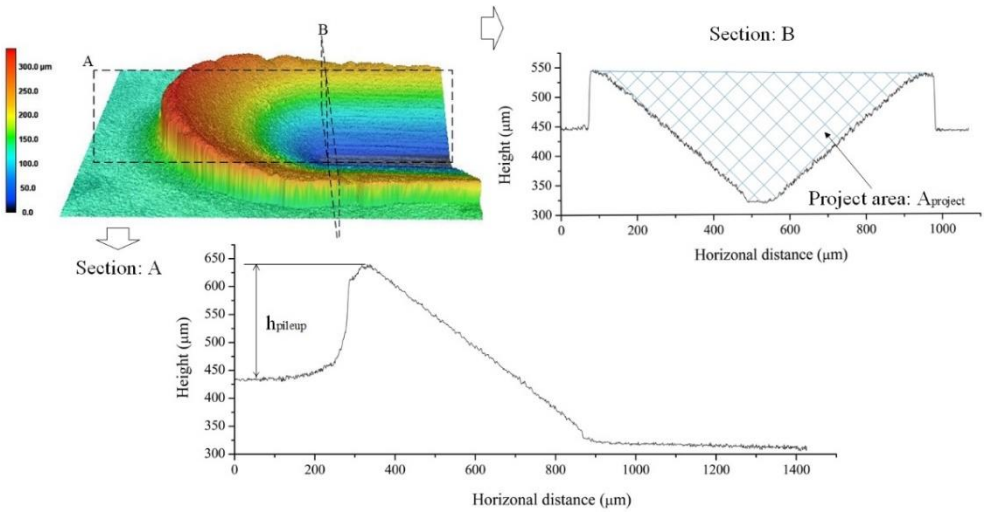

Fig. 16 3D profile measurement of the scratched surface.

4 Validation and Discussion

4.1 Validation of the proposed model

A comparison of the experimental observations and the predicted results were made in this section.

4.1.1 Locations and mechanisms of fracture

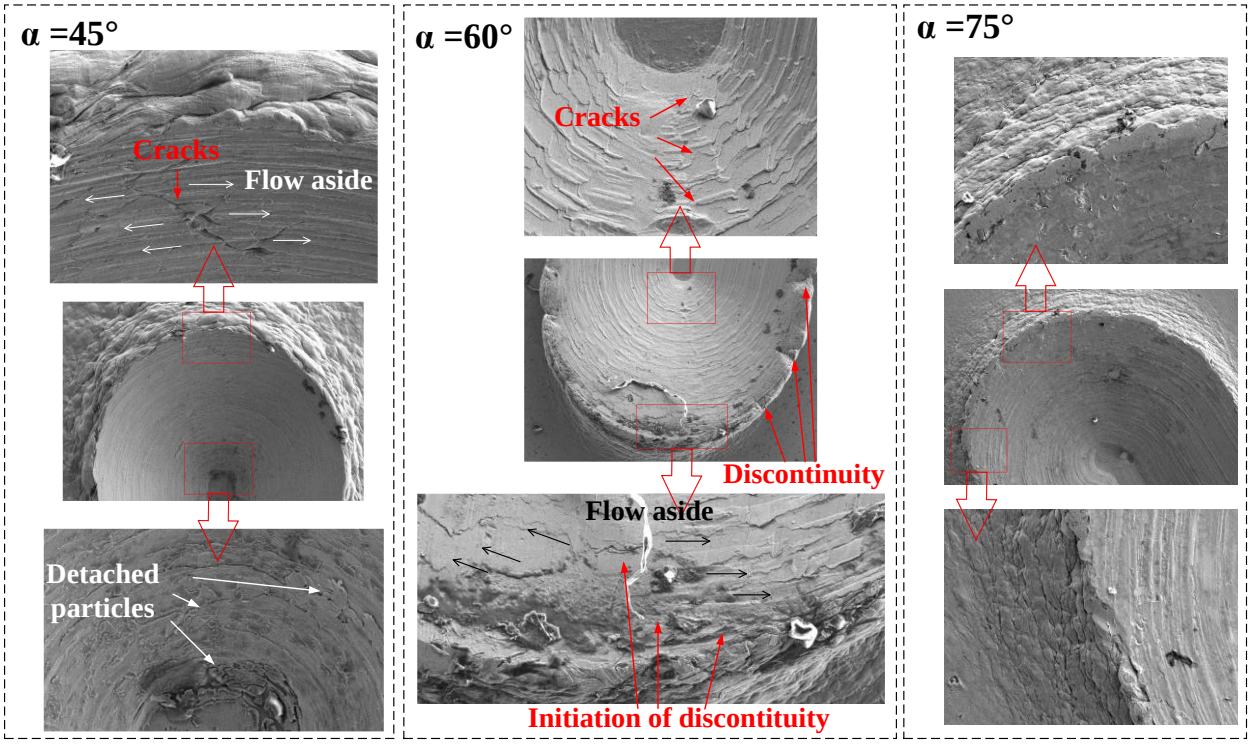

Fig. 17 SEM observation of the scratched surfaces.

Fig. 17 shows the surface morphologies of the samples after scratching tests. For the case with the cone angle α=45°, two different modes of fracture can be observed at different locations of the front ridge. One occurs in the middle of ridge. Long cracks were observed near the symmetry section of trajectory. The shape and location of the cracks indicate that they are caused by the split flow of material in front of the cone, which is in accordance with the analysis based on the developed model as shown in Fig. 14. Those line elements which are not able to climb over the cone would be cut by the cone. Meanwhile, detached cracks can also be found at the bottom of ridge. The lamellar structures indicate that the fracture is caused by the shear stress, which is considered to be the major reason for the fracture behaviors in the scratching process by prior

studies [21, 45]. In these works, the cracks on the surface was considered to begin with the concentration of high compressive stress. Following that the shear fracture occurs. This fracture mode is also in agreement with the predicted results in Fig. 14.

When the cone angle increases to 120° (α=60°), discontinuous flaws can be observed along the side ridges of the groove. More detailed image showed that the flaws comes from the small cracks near the bottom of the ridge. These cracks gradually propagates upwards leading to the discontinuous flaws as a result of the split flow of materials in front of the cone. Thus the fracture in the case with α=60° is mainly caused by the split flow of materials. Notably, lamellar structures can also be observed at the bottom of the ridge, indicating the shear fracture mode also exists in this case. However, the shear cracks are less evident than those observed in the experiments with α=45°. As the cone angle further increases to 150° (with α=75°), no significant discontinuity, crack or detachment can be found, suggesting that the scratching process is dominated by plastic deformation instead of fracture. In summary, it can be found that the dominating fracture mechanism changes from shear failure to tensile fracture with the increase of cone angle. Meanwhile the major initiation location of fracture also changes from the bottom to the middle region of the front ridge. With the further increase of cone angle, no fracture can be found and the scratching process is dominated by plastic deformation. The as-observed experimental scratching behaviors are in good agreement with the predicted results of the developed model as shown in Fig. 14.

4.1.2 Pile up height

The experimental and analytical results of the pile up height after scratching are presented in Fig. 18 for the conditions with the cone angle of 120° and 150°. The calculation was made based on Eq. (88) with the input parameters in Table 2. Both the results show that the pile up height decreases with the increase of the cone angle and grain size. Similar results were reported [24] and they analyzed the pile up ratio of nanocrystalline, ultra-fine crystalline and microcrystalline nickel subject to scratching. Eq. (85) indicates that the pile up height increases with the integrated strain of *Y* direction in the front ridge as shown in Fig. 2. According to Eq. (1), the increase of cone angle leads to the greater strain of material in *Z* direction and smaller strain in *Y* direction. Thus the pile up height decreases with cone angle. In addition, the decrease of pile up height with the increase of grain size could attribute to the variation of plastic hardening behaviors. According to Eq. (3) and Table 1, the ratio of *E/Y* increases with the grain size, which results in a greater deformation region and a smaller overall strain.

Although the predicted results based on the developed model are able to reflect the tendency of pile up height under different scratching conditions, an evident underestimation can be observed by comparing to the experimental results. It may be due to the effect of adhesion on the contacting interface, which is neglected in the model. Our previous studies have revealed that the adhesive force can increase the pile up height in the scratching process. Moreover, with the increase of cone angle, the adhesive effect become more significant [13]. That could be the reason for the closer estimation of pile up ratio with the cone angle of 120° than 150°.

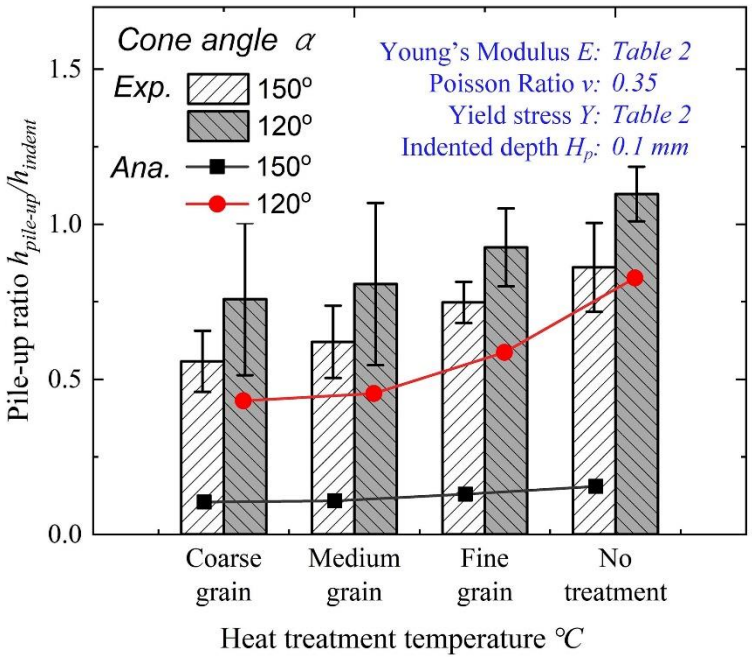

Fig. 18 The pile-up height in front of the rigid cone.

4.2 Critical angles for the transformation of damage mechanism in the scratching process

It has been revealed that the damage mechanism in the scratching process transforms from cracking to plastic deformation with the increase of cone angle [46]. It means that there is a critical cone angle separating the two states. In addition, according to the discussion above, the critical angle is not a constant for different materials, but is affected by the mechanical properties of the tested material. In this section, the critical cone angles for the transformation from plastic deformation to the fracture with different *Y/E* is discussed based on the proposed model.

Based on the calculations made according to the developed model, the damage mechanism is defined as cracking if fracture initiates during the process. The stable state strain distribution in the symmetry section of front ridge of the groove is employed to calculate the critical angle. The

initiation of fracture can be estimated when the equivalent strain is greater than the fracture strain (which can be presented as $\bar{\varepsilon} \geq \bar{\varepsilon}_f$). After that the critical angle is further calculated.

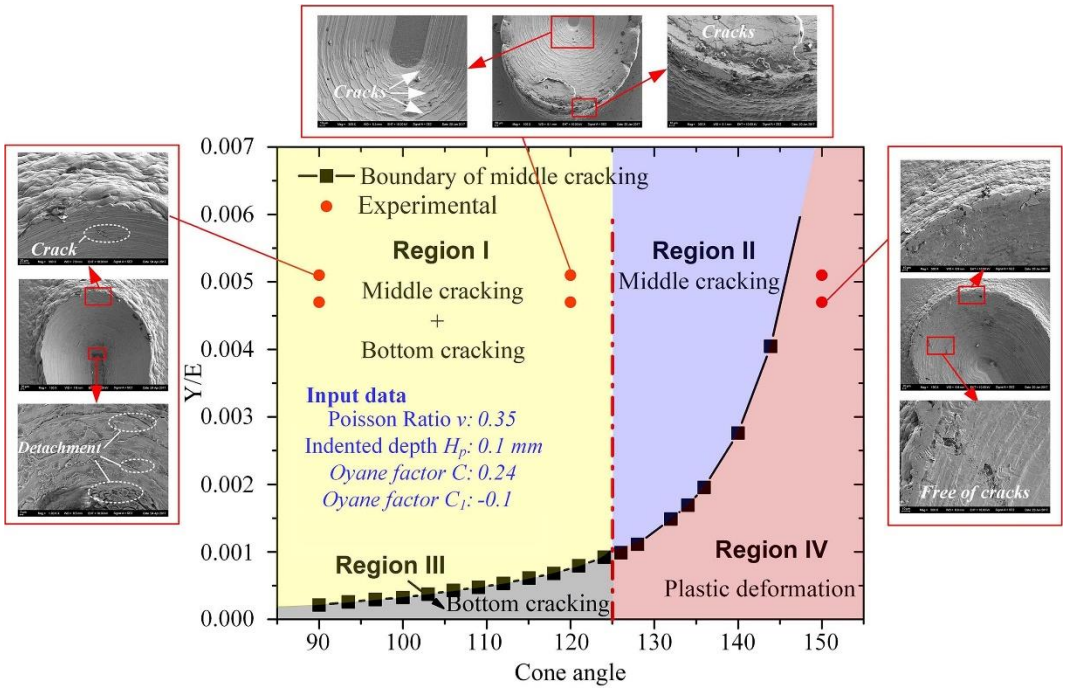

Fig. 19 The map of damage mechanisms in the scratching process.

Fig. 19 shows the map of damage mechanisms in scratching process with the cone angle ranging from 100° to 150°, and the ratio of *Y/E* ranging from 0 to 0.007. The black solid line represents the critical angle for the initiation of cracks in the middle region of the front ridge. If the cone angle is smaller than the critical one (indicated by the area on the left side of the black solid line), cracks could generate in the middle of the front ridge during the scratching process. On the other hand, the crack of material may not occur in that area on the other side of the line since the fracture criterion could not be satisfied. In addition, the critical angle is revealed to increase with *Y/E*, suggesting that cracks are more likely to occur in the middle region of the front ridge with the increase of *Y/E* for a given cone angle.

Furthermore, the red dashed line in Fig. 19 represents the critical angle for the initiation of cracks at the bottom of the front ridge. Obviously, this angle is not affected by *Y/E*, indicating that cracks at the bottom of ridge may occur if the cone angle is smaller than the critical one (as represented by the left hand side of the dashed line) regardless of the *Y/E* values of different materials. The predicted angle is around 125° with the given parameters (*C=0.24, C_1=-0.1, r=10%*). It can explain the results in the prior studies [8], where the critical angle was revealed to be in the range from 121° to 125°.

Therefore, the map can be divided into four regions by the two lines as shown in Fig. 19. In Region I, cracks are predicted to generate in both the bottom and middle regions of the front ridge during the scratching process. In Regions II and III, however, cracks are estimated to occur in the middle and the bottom areas respectively. Nevertheless, no cracks may initiate in Region IV during the scratching process, indicating that plastic deformation is the dominate behavior under that condition. Thus the prior models of scratching process can be distributed to different regions of the map based on its basic assumptions. Akono's model[4] can be applied to the cases in Region I and III, since small cracks were assumed at the bottom of the front ridge. Wang's model [21] can be applied in Region III, due to the assumption that the velocity discontinuity was located in the middle of the front ridge, where the plow mode transformed into cutting mode. Those slip line methods [16] and FE models [24, 47] which consider the material as a continuum during the process should be applied to Region IV, where no fracture generates. The upper boundary method can be applied to all the cases, but more detailed assumptions of velocity discontinuity should be proposed for different regions.

It should be noted that the present study is still a preliminary discussion on the critical angle even though the overview of the transformation of damage mechanisms during the cone scratching process was captured based on the developed model. Many details such as the adhesive force, ductile fracture parameters of C, C_1 and so on have not be well addressed. Further investigations are thus required to characterize these factors on the scratching behaviors. In addition, the surficial micro cracks have been revealed to affect the roughness, quality, fatigue resistance, etc. of workpiece in machining and forming processes. However, due to complex nature of interfacial micro asperities between the tool and the workpiece, a detailed analytical methodology is essential. The model developed in this work could be useful in the process design and optimization towards avoidance of any surficial damages. The model could be incorporated into the data-driven machine learning methods by providing a detailed description of the material flow and fracture behaviors under different scratching conditions. The method could be a valuable solution by avoiding the element distortion and the considerable calculation time in simulations.

5 Conclusions

An analytical frame work is developed in this study to study the damage mechanisms of material in single-cone scratching process. The following concluding remarks can be drawn accordingly.

1) An analytical model was established based on the assumptions of volume constancy and adhesion-free contact. By taking the advantages of small displacement and iteration, the strain distribution and pileup ratio in the symmetry section of the front ridge with different cone angles and material properties of Y/E can be calculated based on the developed model.

2) Considering the ductile fracture criterion, the mechanism and the initiation location of fracture in the scratching process can be predicted. And the prediction is validated by the SEM observations of the scratched grooves. Two fracture mechanisms are found in the scratching process. The bottom cracking initiates at the bottom of the front ridge, and is caused by the maximum shear stress. The middle cracking takes place in the middle of the front ridge, which is attribute to the split flow of materials.
3) With increase of cone angle and Y/E, the initiation location of fracture changes from the bottom to the middle region of ridge. With the further increase of the cone angle and Y/E, no fracture is predicted to occur during the process. The predicted trend is in agreement with experimental observations.
4) A map of damage mechanisms of material is obtained by applying the developed model. Four regions of different facture states are captured to present an overview of the damage mechanisms during the scratching process. The results are in agreement with the previous researches on the scratching behaviors which could be distributed in the four regions.

Acknowledgments

This work was carried out within the projects supported by the National Natural Science Foundation of China (No. 51975363, No. 51905342, No. 51835011, No. U1809220). It was also funded by the Shanghai Nature Science Foundation (Grant No. 19ZR1425700) and the Shanghai Science and Technology Innovation Action Plan (Grant No. 19511107903). Their supports are gratefully appreciated by the authors.

References

[1] Akono, A.T., and Ulm, F.J., 2011, "Scratch test model for the determination of fracture toughness," Engineering Fracture Mechanics, 78(2), pp. 334-342.

[2] Lee, K., Marimuthu, K.P., Kim, C.-L., and Lee, H., 2018, "Scratch-tip-size effect and change of friction coefficient in nano/micro scratch tests using XFEM," Tribology International, 120, pp. 398-410.

[3] Zhao, H., Zhong, Y., and Ma, Z., 2016, "Effects of indentation depth on micro hardness and scratch behavior of thin composite laminate," Journal of Alloys and Compounds, 680, pp. 105-108.

[4] Akono, A.T., and Ulm, F.J., 2012, "Fracture scaling relations for scratch tests of axisymmetric shape," Journal of the Mechanics and Physics of Solids, 60(3), pp. 379-390.

[5] Chen, X., Öpöz, T.T., and Oluwajobi, A., 2017, "Analysis of Grinding Surface Creation by Single-Grit Approach," Journal of Manufacturing Science and Engineering, 139(12).

[6] Wredenberg, F., and Larsson, P.-L., 2009, "Scratch testing of metals and polymers: experiments and numerics," Wear, 266(1), pp. 76-83.

[7] Cao, J., Wu, Y., Lu, D., Fujimoto, M., and Nomura, M., 2014, "Material removal behavior in ultrasonic-assisted scratching of SiC ceramics with a single diamond tool," International Journal of Machine Tools and Manufacture, 79, pp. 49-61.

[8] Sedriks, A., and Mulhearn, T., 1963, "Mechanics of cutting and rubbing in simulated abrasive processes," Wear, 6(6), pp. 457-466.

[9] Zhang, Y., Li, C., Ji, H., Yang, X., Yang, M., Jia, D., Zhang, X., Li, R., and Wang, J., 2017, "Analysis of grinding mechanics and improved predictive force model based on material-removal

and plastic-stacking mechanisms," International Journal of Machine Tools & Manufacture, 122, pp. 67-83.

[10] Mishra, T., de Rooij, M., Shisode, M., Hazrati, J., and Schipper, D. J., 2019, "An analytical model to study the effect of asperity geometry on forces in ploughing by an elliptical asperity," Tribology International, 137, pp. 405-419.

[11] Kato, K., 1992, "Micro-mechanisms of wear—wear modes," Wear, 153(1), pp. 277-295.

[12] Leroch, S., Varga, M., Eder, S. J., Vernes, A., Ripoll, M. R., and Ganzenmueller, G., 2016, "Smooth particle hydrodynamics simulation of damage induced by a spherical indenter scratching a viscoplastic material," International Journal of Solids and Structures, 81, pp. 188-202.

[13] Williams, J., 1996, "Analytical models of scratch hardness," Tribology international, 29(8), pp. 675-694.

[14] Gao, C., and Liu, M., 2019, "Effects of Normal Load on the Coefficient of Friction by Microscratch Test of Copper with a Spherical Indenter," Tribology Letters, 67(1).

[15] Challen, J., and Oxley, P., 1979, "An explanation of the different regimes of friction and wear using asperity deformation models," Wear, 53(2), pp. 229-243.

[16] Yin, X., and Komvopoulos, K., 2012, "A slip-line plasticity analysis of sliding friction of rough surfaces exhibiting self-affine (fractal) behavior," Journal of the Mechanics and Physics of Solids, 60(3), pp. 538-555.

[17] Qiu, Z., Liu, C., Wang, H., Yang, X., Fang, F., and Tang, J., 2016, "Crack propagation and the material removal mechanism of glass–ceramics by the scratch test," Journal of the mechanical behavior of biomedical materials, 64, pp. 75-85.

[18] Duan, N., Yu, Y., Wang, W., and Xu, X., 2017, "Analysis of grit interference mechanisms for the double scratching of monocrystalline silicon carbide by coupling the FEM and SPH," International Journal of Machine Tools and Manufacture, 120, pp. 49-60.

[19] Azarkhin, A., and Devenpeck, M. L., 1997, "Enhanced model of a plowing asperity," Wear, 206(1–2), pp. 147-155.

[20] Linke, B. S., Garretson, I., Torner, F., and Seewig, J., 2017, "Grinding Energy Modeling Based on Friction, Plowing, and Shearing," Journal of Manufacturing Science and Engineering, 139(12).

[21] Wang, H., and Subhash, G., 2002, "Mechanics of mixed-mode ductile material removal with a conical tool and the size dependence of the specific energy," Journal of the Mechanics and Physics of Solids, 50(6), pp. 1269-1296.

[22] Bucaille, J.L., and Felder, E., 2002, "Finite-element analysis of deformation during indentation and scratch tests on elastic-perfectly plastic materials," Philosophical Magazine A, 82(10), pp. 2003-2012.

[23] Subhash, G., and Zhang, W., 2002, "Investigation of the overall friction coefficient in single-pass scratch test," Wear, 252(1-2), pp. 123-134.

[24] Bellemare, S., Dao, M., and Suresh, S., 2007, "The frictional sliding response of elasto-plastic materials in contact with a conical indenter," International Journal of Solids and Structures, 44(6), pp. 1970-1989.

[25] Zhang, T., Jiang, F., Yan, L., and Xu, X., 2018, "Research on the Size Effect of Specific Cutting Energy Based on Numerical Simulation of Single Grit Scratching," Journal of Manufacturing Science and Engineering, 140(7).

[26] Elwasli, F., Zemzemi, F., Mkaddem, A., Mzali, S., and Mezlini, S., 2015, "A 3D multi-scratch test model for characterizing material removal regimes in 5083-Al alloy," Materials & Design, 87, pp. 352-362.

[27] Wang, H., Ning, F., Li, Y., Hu, Y., and Cong, W., 2019, "Scratching-induced surface characteristics and material removal mechanisms in rotary ultrasonic surface machining of CFRP," Ultrasonics, 97, pp. 19-28.

[28] Zheng, X., Zhu, H., Kiet Tieu, A., and Kosasih, B., 2013, "A molecular dynamics simulation of 3D rough lubricated contact," Tribology International, 67, pp. 217-221.

[29] Shugurov, A., Panin, A., Dmitriev, A., and Nikonov, A., 2018, "The effect of crystallographic grain orientation of polycrystalline Ti on ploughing under scratch testing," Wear, 408-409, pp. 214-221.

[30] James, S., and Sundaram, M., 2017, "A Molecular Dynamics Simulation Study of Material Removal Mechanisms in Vibration Assisted Nano Impact-Machining by Loose Abrasives," Journal of Manufacturing Science and Engineering, 139(8).

[31] De Vathaire, M., Delamare, F., and Felder, E., 1981, "An upper bound model of ploughing by a pyramidal indenter," Wear, 66(1), pp. 55-64.

[32] Popov, V. L., 2010, Contact mechanics and friction, Springer.

[33] Rovinelli, A., Sangid, M. D., Proudhon, H., and Ludwig, W., 2018, "Using machine learning and a data-driven approach to identify the small fatigue crack driving force in polycrystalline materials," npj Computational Materials, 4(1), p. 35.

[34] Li, X., Roth, C. C., and Mohr, D., 2019, "Machine-learning based temperature- and rate-dependent plasticity model: Application to analysis of fracture experiments on DP steel," International Journal of Plasticity, 118, pp. 320-344.

[35] Moore, B. A., Rougier, E., O'Malley, D., Srinivasan, G., Hunter, A., and Viswanathan, H., 2018, "Predictive modeling of dynamic fracture growth in brittle materials with machine learning," Computational Materials Science, 148, pp. 46-53.

[36] Pandya, K. S., Roth, C. C., and Mohr, D., 2020, "Strain rate and temperature dependent fracture of aluminum alloy 7075: Experiments and neural network modeling," International Journal of Plasticity, 135, p. 102788.

[37] Bucaille, J. L., Felder, E., and Hochstetter, G., 2001, "Mechanical analysis of the scratch test on elastic and perfectly plastic materials with the three-dimensional finite element modeling," Wear, 249(5–6), pp. 422-432.

[38] Oyane, M., Sato, T., Okimoto, K., and Shima, S., 1980, "Criteria for ductile fracture and their applications," Journal of Mechanical Working Technology, 4(1), pp. 65-81.

[39] Ran, J.Q., and Fu, M.W., 2014, "A hybrid model for analysis of ductile fracture in micro-scaled plastic deformation of multiphase alloys," International Journal of Plasticity, 61, pp. 1-16.

[40] Li, H., Fu, M.W., Lu, J., and Yang, H., 2011, "Ductile fracture: experiments and computations," International journal of plasticity, 27(2), pp. 147-180.

[41] von Stebut, J., Rezakhanlou, R., Anoun, K., Michel, H., and Gantois, M., 1989, "Major damage mechanisms during scratch and wear testing of hard coatings on hard substrates," Thin Solid Films, 181(1–2), pp. 555-564.

[42] Deuis, R. L., Subramanian, C., and Yellup, J. M., 1996, "Abrasive wear of aluminium composites—a review," Wear, 201(1–2), pp. 132-144.

[43] Peng, L.F., Mao, M.Y., Fu, M.W., and Lai, X.M., 2016, "Effect of grain size on the adhesive and ploughing friction behaviours of polycrystalline metals in forming process," International Journal of Mechanical Sciences, 117, pp. 197-209.

[44] Mao, M., Peng, L., Yi, P., and Lai, X., 2016, "Modeling of the friction behavior in metal forming process considering material hardening and junction growth," Journal of tribology, 138(1), p. 012202.

[45] Vyas, A., and Shaw, M. C., 1999, "Mechanics of Saw-Tooth Chip Formation in Metal Cutting," Journal of Manufacturing Science and Engineering, 121(2), pp. 163-172.

[46] Li, K., Shapiro, Y., and Li, J., 1998, "Scratch test of soda-lime glass," Acta materialia, 46(15), pp. 5569-5578.

[47] Krop, S., Meijer, H.E., and van Breemen, L.C., 2016, "Finite element modeling and experimental validation of single-asperity sliding friction of diamond against reinforced and non-filled polycarbonate," Wear, 356, pp. 77-85.